

# REPORT DOCUMENTATION PAGE

AFRL-SR-AR-TR-04-

0146

Public reporting burden for this collection of information is estimated to average 1 hour per response, including the time for reviewing instructions, data needed, and completing and reviewing this collection of information. Send comments regarding this burden estimate or any other aspect of this burden to Department of Defense, Washington Headquarters Services, Directorate for Information Operations and Reports (OIA-04-188-4302). Respondents should be aware that notwithstanding any other provision of law, no person shall be subject to any penalty for failing to valid OMB control number. PLEASE DO NOT RETURN YOUR FORM TO THE ABOVE ADDRESS.

1. REPORT DATE (DD-MM-YYYY)	2. REPORT TYPE		3. DATES COVERED (From - To)	
29-02-2004	Final		1 June 2002 - 30 November 2003	
4. TITLE AND SUBTITLE			5a. CONTRACT NUMBER	
EQUIPMENT FOR AERO-OPTICAL FLOW IMAGING			5b. GRANT NUMBER F49620-02-1-0277	
6. AUTHOR(S)			5c. PROGRAM ELEMENT NUMBER	
Catrakis, Haris, J.			5d. PROJECT NUMBER	
			5e. TASK NUMBER	
			5f. WORK UNIT NUMBER	
7. PERFORMING ORGANIZATION NAME(S) AND ADDRESS(ES)			8. PERFORMING ORGANIZATION REPORT NUMBER	
Prof. Haris J. Catrakis, Principal Investigator Aeronautics and Fluid Dynamics Laboratories University of California, Irvine 4200 Engineering Gateway Irvine, CA 92697-3975				
9. SPONSORING / MONITORING AGENCY NAME(S) AND ADDRESS(ES)			10. SPONSOR/MONITOR'S ACRONYM(S)	
Dr. Thomas J. Beutner, Program Manager Turbulence and Rotating Flows Air Force Office of Scientific Research 4015 Wilson Boulevard, Room 713 Arlington, VA 22203-1954			11. SPONSOR/MONITOR'S REPORT NUMBER(S)	
12. DISTRIBUTION / AVAILABILITY STATEMENT				
Unlimited distribution				
<b>DISTRIBUTION STATEMENT A</b> Approved for Public Release Distribution Unlimited				
13. SUPPLEMENTARY NOTES				
20040311 062				
14. ABSTRACT				
The AFOSR/DURIP Grant has provided the funds to develop a new Aero-Optics Laboratory at UC Irvine, in order to do basic research on aero-optical laser beam propagation through high-speed turbulent flows. The centerpiece of the laboratory is the Aero-Optics Pressurized Flow Facility which is a blow-down wind tunnel especially suited to studies of separated turbulent flows such as the single-stream shear layer. The main pressure vessel can be pressurized to 20 atmospheres, has an internal diameter of 4 feet, an internal height of 8 feet, 5 windows each of 10" diameter and 3.25" thickness made of spectrosil quartz (which permits both visible and UV flow/beam imaging), and 5 window-retaining units capable of 20-atm pressure. The air supply reservoir is rated at 200 gallons and 3,000 psig (~ 200 atm). The facility allows for seeding of air with gaseous acetone. Instrumentation for simultaneous flow/beam imaging includes a custom high-resolution Hartmann sensor, with 4,096 pixels and 1,024 subapertures, and a high-resolution high-sensitivity CCD camera with approximately 1,000 x 1,000 pixels and 12 bits of dynamic range per pixel. A Nd:YAG pulsed laser provides the illumination source with approximately 100 mJ per pulse at a repetition frequency of 10 Hz. Flow durations are of the order of 2 seconds at high subsonic speeds. The facility is designed to reach a Mach number of 2.5 and Reynolds number of approximately 100 million based on the large-scale shear-layer extent.				
15. SUBJECT TERMS				
Large-scale and small-scale aero-optical distortions, high compressibility, large Reynolds numbers, tactical fighter aircraft, laser beam propagation, optical imaging, refractive turbulent fluid interfaces, aero-optical wavefronts, interfacial-thickness				
16. SECURITY CLASSIFICATION OF:		17. LIMITATION OF ABSTRACT	18. NUMBER OF PAGES	19a. NAME OF RESPONSIBLE PERSON
U		UU	?	Prof. Haris J. Catrakis
a. REPORT	b. ABSTRACT	c. THIS PAGE		19b. TELEPHONE NUMBER (include area code) (949) 378-7781
U	U	U		

## DEFENSE UNIVERSITY RESEARCH INSTRUMENTATION PROGRAM

AFOSR/DURIP Grant F49620-02-1-0277

## EQUIPMENT FOR AERO-OPTICAL FLOW IMAGING

## Final Report

Grant period: June 1, 2002 to November 30, 2003

Funds awarded from DURIP in this Grant period: \$158,176

Cost-sharing funds from UC Irvine in this Grant period: \$39,544

Total funding for equipment acquired in this Grant period: \$197,720

### AFOSR Program Manager:

Dr. Thomas J. Beutner  
Program Manager  
Turbulence and Rotating Flows  
Aerospace and Materials Sciences Directorate  
Air Force Office of Scientific Research

4015 Wilson Boulevard, Room 713  
Arlington, VA 22203-1954  
Phone: (703) 696-6961  
Fax: (703) 696-8451  
E-mail: [tom\\_beutner@afosr.af.mil](mailto:tom_beutner@afosr.af.mil)

**Principal Investigator:**

Dr. Haris J. Catrakis  
Assistant Professor  
Turbulence and the Dynamics of Fluids  
Aeronautics and Fluid Dynamics Laboratories  
University of California, Irvine

4200 Engineering Gateway  
Irvine, CA 92697-3975  
Phone (office): (949) 824-4028  
Phone (mobile): (949) 378-7781  
E-mail: [catrakis@uci.edu](mailto:catrakis@uci.edu)

February 29, 2004

## **Abstract**

A new Aero-Optics Pressurized Flow Facility was designed and built to support research, defence, and educational objectives in the study of aero-optical interactions in turbulent flows. The equipment purchased as part of this DURIP Grant has produced the new aero-optics Pressurized Flow Facility at the University of California, Irvine, whose goals are: (a) to enable high-resolution laboratory measurements of optical beam propagation in turbulent flows, (b) to contribute to physical understanding, modeling, and control of aero-optical flow phenomena, (c) to contribute to the advancement of Air Force aero-optical applications, and (d) to educate engineering students in aeronautical applications of aero-optics with hands-on laboratory experience. The equipment selected and purchased as part of this laboratory included: a multi-purpose pressure vessel with ample optical access to the interior via five 10-in diameter 3.25-in thick spectrosil quartz windows, an air receiver that can be pressurized up to 3000 psig needed to provide the upstream driving pressure of the blow-down experiments, flow-management devices to regulate the flow, a high-resolution CCD camera used to directly measure the flow field, a pulsed Nd:YAG laser operated in the UV at 266 nm with 100 mJ/pulse at 10 Hz, a gaseous acetone seeding system used to provide the acetone vapor necessary for laser-induced fluorescence techniques, and a real-time data-acquisition computer. The unique design of the aero-optics Pressurized Flow Facility can produce novel high-resolution measurements of aero-optical beam propagation in turbulent flows at large Reynolds numbers. These data are useful for the development of accurate models that predict aero-optical effects and is also useful to computational researchers by providing a database documenting aero-optical effects through measurements. Educationally, the requested equipment provided the opportunity for graduate and undergraduate students to acquire measurement skills useful for the study of aero-optical flow phenomena.

## 1. Introduction

In order to develop techniques for the prediction and control of aero-optical phenomena in turbulent flows, an improved understanding is needed of the large-scale properties and, for some applications, of the small-scale properties of aero-optical distortions as well as of the turbulent refractive fluid interfaces that generate these distortions (e.g. [1] Jumper & Fitzgerald 2001, and references therein). Practically, the large-scale aero-optical behavior is crucial in all applications involving optical beam propagation or imaging through turbulent shear flows, such as the flows generated by airborne vehicles. The small-scale behavior can also be important for those applications that require high-resolution and/or long-range optical imaging or beam propagation. In addition, the behavior of aero-optical interactions at large Reynolds numbers is important and for high-speed flight, it is also crucial to quantify Mach-number effects on the aero-optical behavior (e.g. [2] Gilbert & Otten 1982, and references therein).

The large-scale organized flow behavior is known to provide the dominant aero-optical contributions in both incompressible turbulent flows (e.g. [3] Truman & Lee 1990; [4] Wissler & Roshko 1992; [5] Dimotakis, Catrakis, & Fourguette 2001) and weakly-compressible turbulent flows (e.g. [1] Jumper & Fitzgerald 2001). At higher flow compressibilities, however, the extent to which the large-scale flow behavior is organized is not well understood (e.g. [6] Smits & Dussauge 1996; [5] Dimotakis, Catrakis, & Fourguette 2001). The large-scale properties of aero-optical distortions at high compressibility, and the manner in which they are related to the fluid-interfacial behavior, are also not well understood.

Since the pioneering aero-optics studies by Liepmann (1952 [7], 1952b [8]), it has been recognized that one of the central goals in aero-optics research is to relate the optical-wavefront distortions to the fluid-mechanical behavior. The optical-wavefront distortions are usefully quantified by the optical path length (OPL), here denoted as  $\Lambda(\mathbf{x}, t)$ , for many aero-optics applications. The most relevant fluid-mechanical quantity in aero-optics is the refractive-index field,

$$n(\mathbf{x}, t) \equiv \frac{c_0}{c(\mathbf{x}, t)} \geq 1 , \quad (1)$$

where  $c(\mathbf{x}, t)$  is the local speed of light which is always less than or equal to Einstein's universal speed of light  $c_0$  in vacuum and independent of the frame of reference. In turbulent flows, the refractive-index field  $n(\mathbf{x}, t)$  can be highly nonuniform particularly at large Reynolds numbers and at high compressibility. The propagation of optical wavefronts through refractive-index fields is governed by the eikonal equation,

$$|\nabla \Lambda| = n , \quad (2)$$

where, as stated above,  $\Lambda$  denotes the OPL. The eikonal equation is useful to describe fluid-optical interactions as long as the wavelength of light is smaller than the smallest fluid-mechanical (turbulent) scale and as long as the optical-beam energies are low enough to not change the local refractive index. An experimental flow facility that can enable the simultaneous measurements of turbulent flows and flow-generated optical wavefront distortions is crucial for understanding the aero-optical interactions. Relating the optical-

wavefront distortions to the fluid-mechanical behavior is one of the major goals of the aero-optics Pressurized Flow Facility built in part by this DURIP Grant.

## 2. Description of the New Aero-Optics Pressurized Flow Facility

The new Aero-Optics Pressurized Flow Facility was designed and built to allow direct simultaneous measurements of the flow field and the flow-generated optical wavefront distortions. The ability to simultaneously measure the flow field and the optical wavefronts distortions is one of the most important contributions of the new Aero-Optics Pressurized Flow Facility which is housed in the Aeronautics and Fluid Dynamics Laboratories at the UC Irvine. The new facility shown in the photograph of figure 1 is a pressurized wind tunnel operated in a blow-down configuration. Figure 2 shows a drawing of the driver reservoir vessel, and figure 3 shows a drawing of the main Aero-Optics vessel.

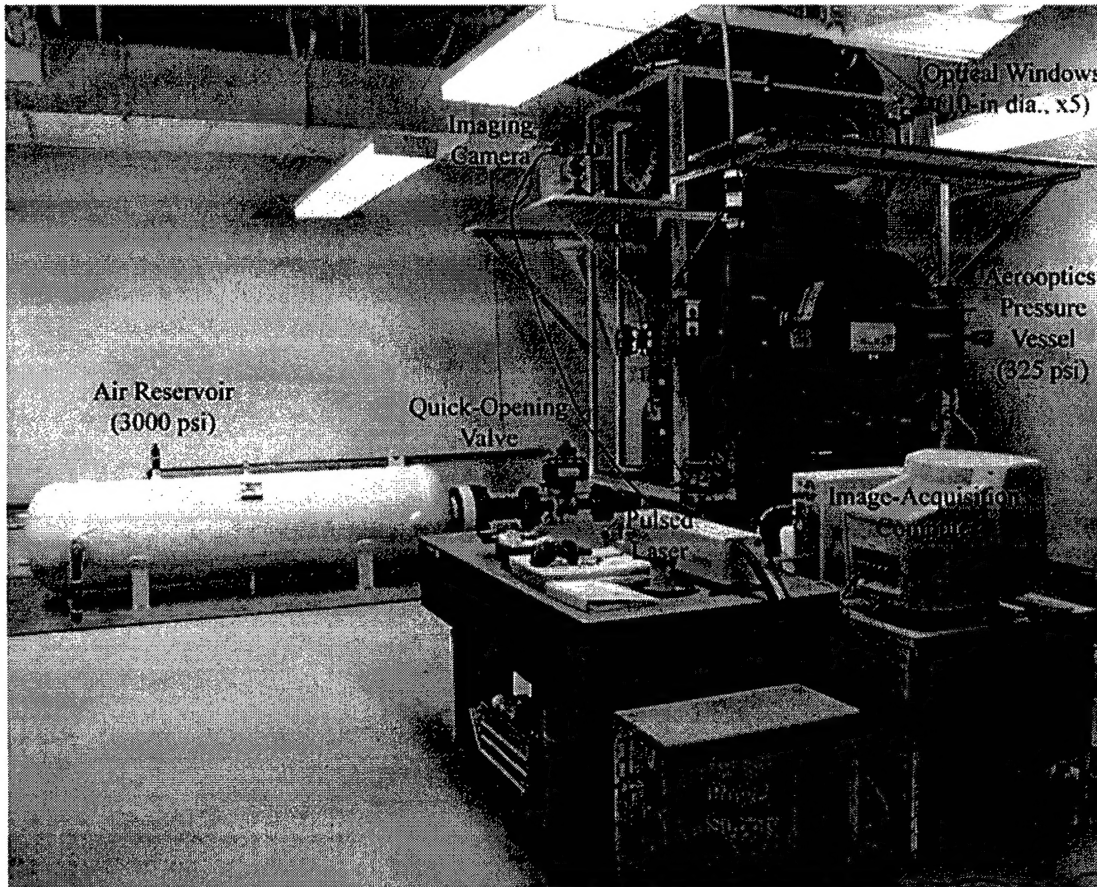


Figure 1: The aero-optics Pressure Vessel at UC Irvine designed for simultaneous imaging of the flow field and the optical wavefront distortions. The facility can generate aero-optical flows at large Reynolds numbers  $Re \sim 10^6 - 10^8$  and over a wide range of compressibilities  $0.15 \lesssim M_c \lesssim 1.0$ .

An air reservoir with an internal volume of 200-gallon was designed according to the ASME Pressure Vessel Code Section VIII Division I and it was issued a U-stamp upon completion of its construction and inspection. A drawing of the air reservoir is shown

in figure 3. The air reservoir has a maximum pressure rating of 3000 psig in order to provide the necessary upstream driving pressure to run experiments at high Reynolds numbers ( $Re \sim 10^6 - 10^8$ ) and across a wide range of compressibilities ( $M_c \sim 0.15 - 1.0$ ). Airflow from the air reservoir to the experiments is delivered through high-pressure 6-inch diameter piping. The facility is operated in a blowdown configuration and the mass flow rate to the experiments is controlled using a pneumatically-actuated fast-acting valve in combination with fixed-area metering devices.

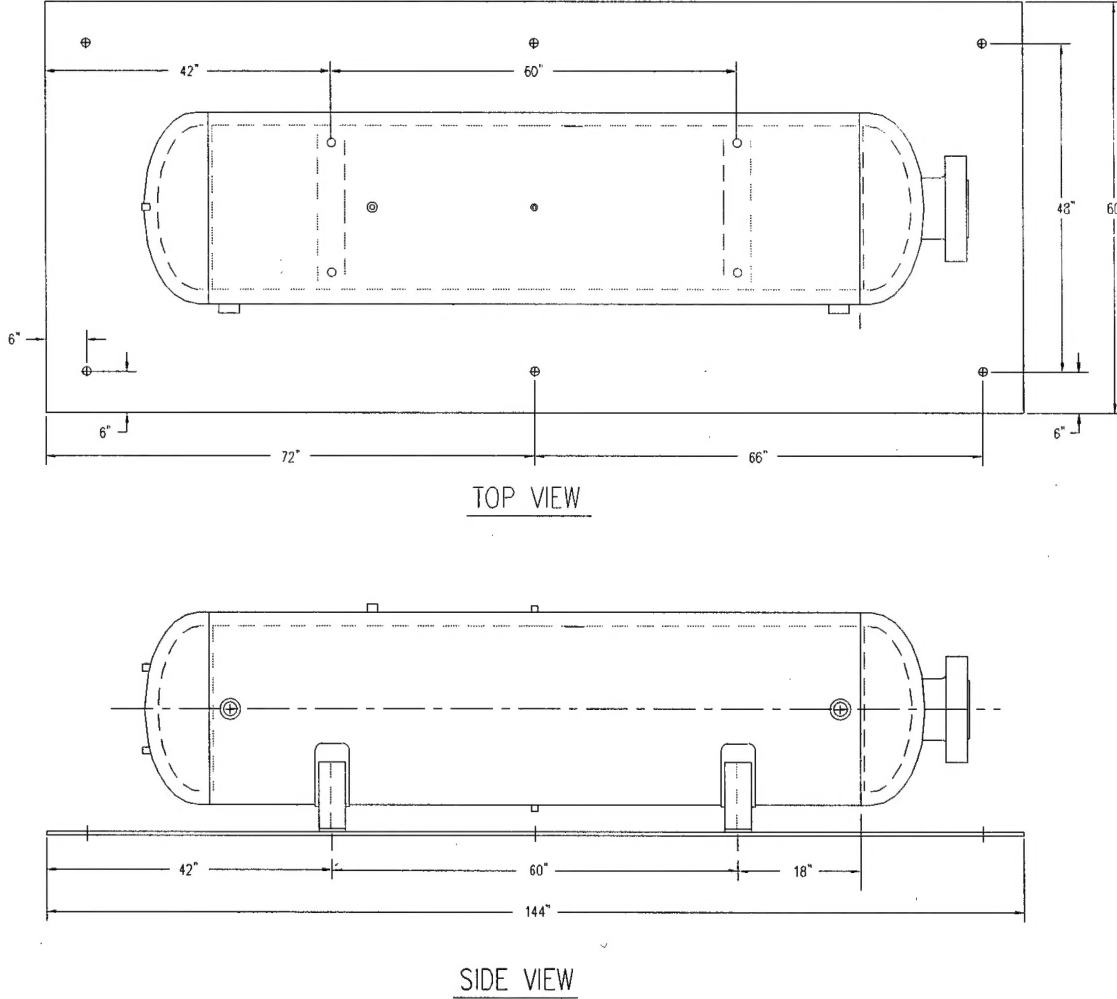


Figure 2: Drawing of the air reservoir which has an internal volume of 200 gallons and can be pressurized up to 3000 psig.

The airflow from the upstream high-pressure air reservoir is received by the aero-optics pressure vessel which has a 4-foot inside diameter and 8-foot internal height. There are two 6-in diameter inlets located on the bottom of the aero-optics vessel and four 2-in outlets located on the top. This aero-optics vessel provides a controlled environment for the experiment's test section with the capability to vary the internal pressure up to a maximum of 325 psig or 20 atm.

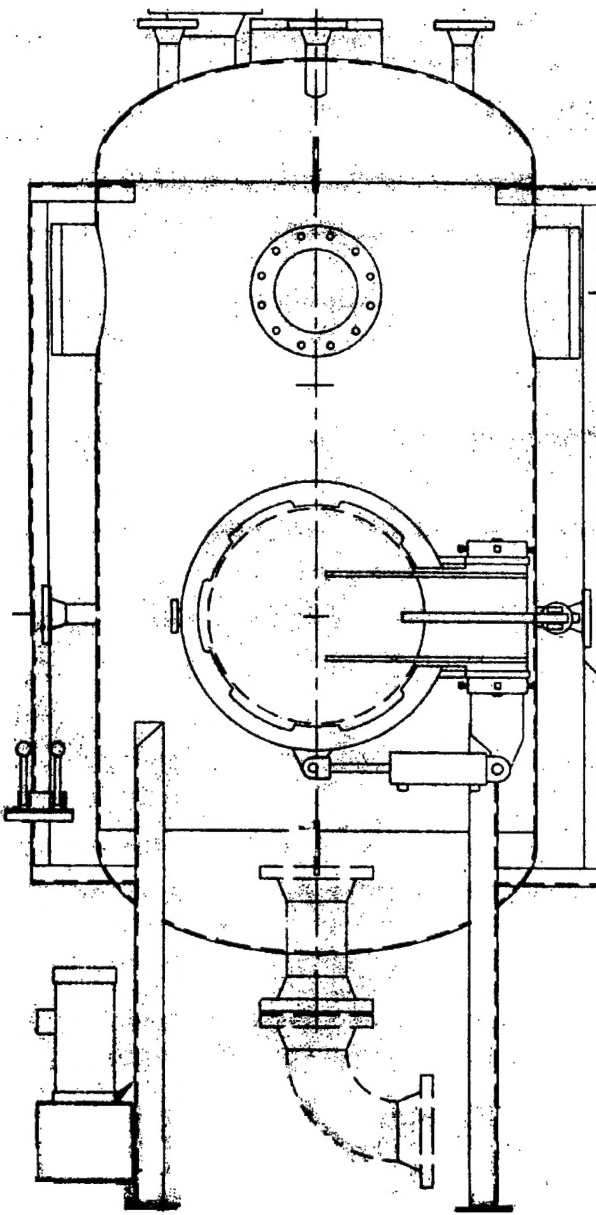


Figure 3: Drawing of the main Aero-Optics vessel with 8-foot internal height and 4-foot inside diameter, with the quick-opening 2-foot diameter door.

The variable pressure capability allows for elevated pressures in the experiment test-section, which enhances the measurable aero-optical effect and the signal-to-noise ratio of the flow and wavefront imaging techniques. A 2-foot diameter custom-designed breach lock type door that is hydraulically operated permits access to the interior of the vessel for the purpose of installing and adjusting the components of the experiment flow tunnel. The door on the side of the aero-optics vessel is equipped with an electronic start/stop station that enables the opening/closing of the door within 10 seconds. In addition, the door includes a safety interlock to prevent the opening of the door when the vessel is pressurized. Optical access to the interior of the aero-optics vessel is enabled through

five  $10.00+/-0.010$  inch diameter  $3.25+/-0.010$  inch thick windows. The material of the windows was chosen to be spectrosil quartz in order to allow more than 90% transmission of ultraviolet laser beams. The spectrosil quartz windows were mounted on the pressure vessel using custom-designed weld units that use compression screws to maintain the windows in place under the maximum pressure rating of 325 psig. The spectrosil quartz windows are polished on both sides to a 40/20 surface finish and a flatness of less than 1/4 waves per inch over 85% of clear aperture.

The aero-optics Pressure Vessel provides a controlled variable pressure environment for the test-section of the experiment. The relatively large size of the aero-optics Pressure Vessel enables the flow tunnel internals to be modified in order to accommodate different flow geometries, e.g. dual-stream shear-layer, single-stream shear-layer in planar and curved configurations. As part of this grant a flow tunnel of the single-stream shear layer was designed and built. The configuration of the single-stream shear layer was designed to generate a subsonic single-stream shear-layer with a splitter-plate test-section exit height of 3 inches and a span of 12 inches as shown in figure 4. This configuration allows for a comprehensive study of a separated flow of practical relevance for aero-optics where the effects of Mach number, Reynolds number, and density-ratio may be isolated. High-Reynolds number ( $Re \sim 10^6 - 10^8$ ) and high-Mach number ( $M_c \sim 1.0$ ) flows are attainable with the current single-stream shear-layer configuration.

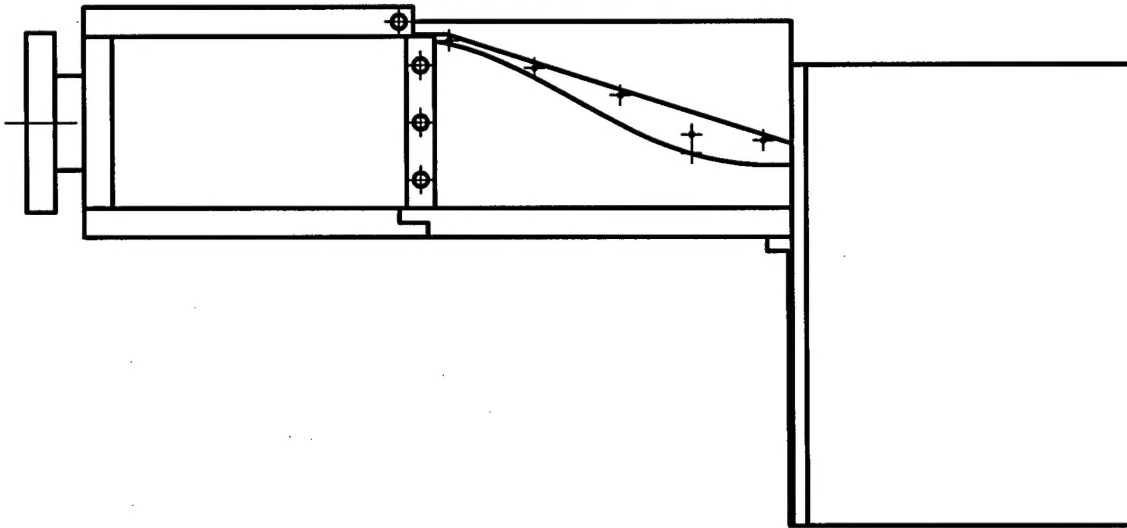


Figure 4: Schematic of the single-stream shear-layer tunnel insert used to generate the separated turbulent shear layer, shown in the subsonic configuration.

A single-stream shear-layer tunnel with a test-section entrance area of 3-inch x 12-inch is contained inside the main pressurized vessel. The configurations of the single-stream and dual-stream shear layers share many design aspects. The current configuration of the single-stream shear layer consists of a 12-inch x 12-inch flow management section, which contains two sets of metal screens and two sets of honeycomb sections. For subsonic experiments, after the honeycomb sections a converging nozzle leads the flow to the test section entrance of 3-inch height x 12-inch span. To meet the flow requirements

of supersonic experiments, the flow management section and contraction section are adaptable to geometrically smaller cross-sections that also include a converging-diverging nozzle. The test section consists of two fixed sidewalls and an adjustable guidewall that spans the 2-foot length of the test-section. The fourth plane of the test section is open without restrictions in order to allow entrainment of the surrounding ambient air. As shown in figure 3, an entrainment wall is positioned near the test-section entrance in order to provide near-field boundary conditions consistent with previous studies. The test-section boundary conditions of the single-stream shear layer provide a favorable geometry for the maximum growth of separated layers that begin to form at the entrance of the test-section. The maximum growth rate is a favorable characteristic of separated shear layers in terms of capturing the flow structure using digital imaging techniques.

A pulsed Nd:YAG laser provides the illumination source needed for the measurement of the flow images and the optical wavefront distortions. The Nd:YAG laser is a Spectra-Physics INDI model equipped with a fourth-harmonic generator that enables its operation in the ultraviolet range at 266-nm. The energy output is / 100 mJ/pulse at a repetition rate of 10 Hertz. High-quality optical mirrors and laser-sheet-forming optics with anti-reflective coatings are placed externally to the laser to guide the optical beam to the experiment's test section through the spectrosil quartz windows.

### **3. Facility Operation for Quantitative Aero-Optical Imaging**

The flow facility and shear layer tunnel configuration described above are used to generate a separated flow with the maximum growth rate. The optical wavefront distortions can be measured directly by employing a Shack-Hartmann wavefront sensor. Direct quantitative measurements of the density field may be achieved using laser-imaging techniques such as planar laser-induced fluorescence (PLIF) of acetone vapor. However, the relatively high signal obtained from laser fluorescence of acetone vapor compared to other imaging techniques makes it a prospective candidate for flow imaging of separated flows (Lozano, Yip, & Hanson 1992 [9]). A density-field imaging technique is proposed using laser-induced fluorescence of acetone where calibrated concentrations of seeded acetone vapor are introduced in the freestream and in the test-section ambient air. The calibrated concentrations of the two streams allows for direct measurements of intensity variations due to compressibility effects without the influence of molecular mixing. This density imaging technique provides a means for separating the effects of molecular mixing of dissimilar gases from the effects observed due to air compressibility at high speeds.

The objective of this flow imaging technique is to directly relate the captured flow images of acetone fluorescence to the index-of-refraction flow field. The method for obtaining the density flow field consists of forming the output beam of a Nd:YAG pulsed laser into a thin two-dimensional laser sheet. The Nd:YAG laser is operated in UV mode at a wavelength of 266-nm in order to remain within the absorption spectrum needed for the fluorescence of acetone vapor. The UV laser was operated in 10-Hz mode with typical energy output of 100-mJ per pulse. The concentration of acetone vapor was introduced by means of a metered bubbling process separately to the upstream air reservoir and the test section that is housed inside the aero-optics vessel. This acetone vapor seeding procedure allows for the acetone vapor concentration to be matched in the flowing stream

and in the experiment test section. This acetone seeding technique allows acetone vapor seeding of only one of the streams, which at weakly to highly-compressible flow conditions the effects of turbulent mixing in addition to compressibility may be investigated.

With the present implementation of the acetone fluorescence imaging technique, we have managed to successfully record the first quantitative images of the separated shear layer. For these experiments, the separated shear layer was created using a single-stream shear layer configuration. The results obtained from the single-stream shear layer configuration confirm the expected linear growth rate in the far field as seen in figure 5. The large size of the pressure vessel, which contains the test section, provides ample entrainment and the sharp 90-degree corner is sufficiently large to ensure that the shear layer does not reattach. Images similar to the shear layer shown in figure 3 provide quantitative information on the instantaneous spatial structure of the refractive fluid interfaces in this flow.



Figure 5: Preliminary raw image of the separated shear layer in the UCI aero-optics Flow Facility. Flow is from left to right, and the high-speed freestream is on the top side. The bottom side corresponds to the ambient air in the pressure vessel. Linear growth and large-scale features are evident in this image of the large-Reynolds-number separated shear layer. The dark spots correspond to residual acetone droplets in this preliminary image. These have been eliminated in more recent experiments in our facility by creating purely-gaseous acetone in the freestream and/or in the ambient air in the facility.

The present flow-imaging technique is currently being extended to record directly the density field, and therefore the density interfaces generated in a separated shear layer. This procedure extends the power of laser-induced fluorescence by using a calibrated air/acetone-vapor mixture for the ambient fluid as well as for the freestream in order to capture a quantitative representation of the density field. Since the proposed density whole-field imaging method uses purely gaseous fluid, simultaneous imaging of both the flow and the propagated laser wavefronts is enabled. The optical wavefront distortions will be conducted using a high-resolution spatial Shack-Hartmann sensor. Initial studies of curved separated shear layers are also being conducted in order to explore the use of streamwise flow curvature as a passive means for flow control and reduction of the aero-optical distortions.

The facility enables the simultaneous imaging of the density field and the optical wavefronts through five 10-inch diameter quartz windows which allow optical access to the

interior of the vessel. A new imaging technique is being developed where laser-induced fluorescence of acetone vapor, seeded in the flow in a calibrated way to remove the effects of mixing between dissimilar gas streams, can be used to provide direct measurements of the density field. The concentration of acetone vapor is regulated and introduced to the fully-enclosed experiment freestream and ambient air inside the test section using a liquid bubbling technique. The acetone vapor concentration was maintained in the optically-thin regime. A pulsed Nd:YAG laser operated at a wavelength of 266 nm provides the excitation source for acetone which yields fluorescence in the visible range (350-550 nm). The first flow image of the separated shear layer recorded in the new aero-optics Flow Facility at UC Irvine is shown in figure 5. One of the main objectives of the flow imaging technique is to record high signal-to-noise ratio images that are needed in order to extract information of the refractive interfaces responsible for the aero-optical distortions. A new wavefront sensor is being developed to directly measure the optical wavefronts to provide high spatial resolution of the optical distortions generated by the density field. It is a custom Hartmann UV sensor based on a DALSA Piranha 4,096-pixel 1,024-subaperture detector. This will permit the simultaneous high-resolution beam/flow imaging using the new aero-optics flow facility.

#### 4. Conclusions and Implications

The Aero-Optics Pressurized Flow Facility at UC Irvine is a unique facility that is especially designed for the study of separated flows. It permits simultaneous imaging of both the flow and beam behavior. This facility is expected to produce archival results of aero-optical interactions and to provide a testing environment for exploring flow-control techniques and optical-control techniques to reduce aero-optical distortions. The anticipated flow/beam images will provide a high-resolution database which can be analyzed to determine both the large-scale and small-scale aero-optical behavior at large Reynolds numbers, with compressibility effects, using the new Interfacial-Fluid-Thickness framework developed by the PI under previous AFOSR support (Catrakis & Aguirre 2004 [10], *AIAA Journal*, accepted for publication; Catrakis, Aguirre, & Nathman [11], *AIAA Journal*, accepted for publication).<sup>1</sup>

## References

- [1] E. J. Jumper and E. J. Fitzgerald. Recent advances in aero-optics. *Prog. Aerospace Sci.*, 37:299–339, 2001.
- [2] K. G. Gilbert and L. J. Otten. Aero-optical phenomena. In *Progress in Astronautics and Aeronautics*, volume 80. American Institute of Aeronautics and Astronautics, 1982.

---

<sup>1</sup>AFOSR Grant F49620-02-1-0142, 03/01/2002 - 08/31/2002, Program Manager: Dr. Thomas J. Beutner.

- [3] C. R. Truman and M. J. Lee. Effects of organized turbulence structures on the phase distortion in a coherent optical beam propagating through a turbulent shear flow. *Phys. Fluids A*, 2:851–857, 1990.
- [4] J. B. Wissler and A. Roshko. Transmission of thin light beams through turbulent mixing layers. In *AIAA 30<sup>th</sup> Aerospace Sciences Meeting*, AIAA-92-0658, Reno, NV, 1992.
- [5] P. E. Dimotakis, H. J. Catrakis, and D. C. L. Fourguette. Flow structure and optical beam propagation in high-Reynolds-number gas-phase shear layers and jets. *J. Fluid Mech.*, 433:105–134, 2001.
- [6] A. J. Smits and J.-P. Dussauge. *Turbulent Shear Layers in Supersonic Flow*. AIP Press, 1996.
- [7] H. W. Liepmann. Aspects of the turbulence problem. Part 2: IV. General discussion, V. Isotropic turbulence,. *Z. angew. Math. Phys.*, 3:407–426, 1952.
- [8] H. W. Liepmann. Deflection and diffusion of a light ray passing through a boundary layer. Douglas Aircraft Company Report SM-14397, Santa Monica, CA, 1952.
- [9] A. Lozano, B. Yip, and R. K. Hanson. Acetone: a tracer for concentration measurements in gaseous flows by planar laser-induced fluorescence. *Exp. in Fluids*, 13:369–376, 1992.
- [10] H. J. Catrakis and R. C. Aguirre. New interfacial-fluid-thickness approach in aerooptics with applications to compressible turbulence. *AIAA J.*, 2004. accepted for publication.
- [11] H. J. Catrakis, R. C. Aguirre, and J. C. Nathman. Aero-optical wavefronts and scale-local characterization in large-Reynolds-number compressible turbulence. *AIAA J.*, 2004. accepted for publication.

## New Interfacial-Fluid-Thickness Approach in Aero-Optics with Applications to Compressible Turbulence

Haris J. Catrakis\* and Roberto C. Aguirre†

*Aeronautics and Fluid Dynamics Laboratories  
University of California, Irvine, CA 92697*

### Abstract

A new approach in aero-optics is proposed based on the physical thickness of refractive fluid interfaces. In turbulent flows, particularly at large Reynolds numbers, the interfacial fluid thickness is highly variable. The role of this interfacial fluid thickness in aero-optical interactions is examined by directly relating the optical path length (OPL) to the interfacial-fluid-thickness (IFT) variations. This is done by expressing the OPL as an integral of the IFT variations along the beam propagation path. We demonstrate the proposed IFT approach on refractive-field measurements in large-Reynolds-number ( $Re \sim 10^6$ ) high-compressibility ( $M_c \sim 1$ ) shear layers between optically-different gases. Highly-irregular networks of isolated high-gradient interfaces are observed at various transverse locations in the flow, i.e. both in the interior and near the outer boundaries. The observation that the high-gradient interfaces are spatially isolated, and the OPL interpretation in terms of the IFT variations, are utilized to propose and demonstrate a new modeling approach for compressible flow where the high-gradient interfaces are the dominant elements needed to capture the large-scale optical distortions. The present approach suggests a new point of view for relating aero-optical distortions to the flow structure in terms of the IFT variations.

### 1. Introduction

In order to develop techniques for the prediction and control of aerooptical phenomena in turbulent flows, an improved understanding is needed of the large-scale properties and, for some applications, of the small-scale properties of aerooptical distortions as well as of the turbulent refractive fluid interfaces that generate these distortions (e.g. Jumper & Fitzgerald<sup>1</sup> and references therein). Practically, the large-scale aerooptical behavior is crucial in all

---

\*Assistant Professor, Member AIAA, Corresp. Author, E-mail: catrakis@uci.edu, Tel: (949) 378-7781.

†Graduate Student, Member AIAA.

applications involving optical beam propagation or imaging through turbulent shear flows, such as the flows generated by airborne vehicles. The small-scale behavior can also be important for those applications that require high-resolution and/or long-range optical imaging or beam propagation. In addition, it is important to know in practice the behavior of aero-optical interactions at large Reynolds numbers. Furthermore, for high-speed flight, it is also crucial to quantify Mach-number effects on the aerooptical behavior (e.g. Gilbert & Otten<sup>2</sup> and references therein).

The large-scale organized flow behavior is known to provide the dominant aerooptical contributions in both incompressible turbulent flows (e.g. Truman & Lee<sup>3</sup>; Wissler & Roshko<sup>4</sup>; Dimotakis, Catrakis, & Fourguette<sup>5</sup>) and weakly-compressible turbulent flows (e.g. Jumper & Fitzgerald<sup>1</sup>). At higher flow compressibilities, however, the extent to which the large-scale flow behavior is organized is not well understood (e.g. Smits & Dussauge<sup>6</sup>; Dimotakis, Catrakis, & Fourguette<sup>5</sup>). The large-scale properties of aerooptical distortions at high compressibility, and the manner in which they are related to the fluid-interfacial behavior, are also not well understood.

In the present work, we propose an approach to examine aerooptical interactions in terms of the variations in the thickness of refractive fluid interfaces. Refractive interfaces physically exhibit a thickness given by the inverse of the refractive-index gradient magnitude. This interfacial-fluid-thickness can be highly nonuniform in turbulent flows, particularly at large Reynolds numbers. The interfacial-fluid-thickness variations play an important role in aerooptics. In §2, we describe the interfacial-fluid-thickness (IFT) approach and show that the optical path length (OPL) can be expressed directly in terms of the variations in interfacial fluid thickness. In §3, we demonstrate this approach on high-compressibility large-Reynolds-number shear layers of optically-different gases. The high-gradient interfaces are identified and their behavior is compared to the case of low compressibility. A discussion is included on the issue of mixing vs. compressibility effects. In §4, we propose and demonstrate a new modeling approach in which the high-gradient interfaces are used to produce the large-scale aerooptical distortions at high compressibility. In a companion work, we examine the small-scale behavior of aerooptical distortions at high compressibility and large Reynolds numbers, by means of a new method for characterizing the scale-local structure of optical wavefronts (Catrakis, Aguirre, & Nathman<sup>7</sup>).

## 2. Proposed interfacial-fluid-thickness (IFT) approach in aero optics

Since the pioneering aero optics studies by Liepmann<sup>8,9</sup>, it has been recognized that one of the central goals in aero optics research is to relate the optical-wavefront distortions to the fluid-mechanical behavior. The optical-wavefront distortions are usefully quantified by the optical path length (OPL), for many aero optics applications. The most relevant fluid-mechanical quantity in aero optics is the refractive-index field,

$$n(\mathbf{x}, t) \equiv \frac{c_0}{c(\mathbf{x}, t)} \geq 1 , \quad (1)$$

where  $c(\mathbf{x}, t)$  is the local speed of light which is always less than or equal to the speed of light  $c_0$  in vacuum. In turbulent flows, the refractive-index field  $n(\mathbf{x}, t)$  can be highly nonuniform particularly at large Reynolds numbers. The propagation of optical wavefronts through refractive-index fields is governed by the eikonal equation, which can be expressed in terms of the OPL as,

$$|\nabla(\text{OPL})| = n . \quad (2)$$

The eikonal equation is useful to describe fluid-optical interactions as long as the wavelength of light is smaller than the smallest fluid-mechanical (turbulent) scale (e.g. Liepmann<sup>9</sup>) and as long as the optical-beam energies are low enough to not change the local refractive index.

How is the OPL behavior related physically to the structure of the refractive-index field and in particular the refractive fluid interfaces? In this section, we present a framework that is useful to address this question by emphasizing the role of the physical thickness of the refractive fluid interfaces in determining the variations in the OPL.

As a starting point, we recall the expression used for the definition of the OPL as an integral of the refractive index along each light ray in geometric optics (e.g. Dimotakis, Catrakis, & Fourguette<sup>5</sup>; Jumper & Fitzgerald<sup>1</sup>, and references therein), i.e.,

$$\text{OPL}(\mathbf{x}, t) \equiv \int_{\text{ray}} n(\ell, t) d\ell , \quad (3)$$

where  $\ell$  denotes the physical distance along the beam propagation path for each light ray. The OPL integral in equation 3 corresponds to inverting the eikonal equation 2 for the OPL in terms of the refractive-index field. The aero optical distortions correspond to the optical-

path difference (OPD) given by  $\text{OPD}(\mathbf{x}, t) \equiv \text{OPL}(\mathbf{x}, t) - \text{OPL}_{\text{ref}}(\mathbf{x}, t)$ , where  $\text{OPL}_{\text{ref}}(\mathbf{x}, t) \equiv \int_{\text{ray}} n_{\text{ref}}(\mathbf{x}, t) d\ell$  is the reference OPL that would correspond to the undistorted wavefronts, with  $n_{\text{ref}}$  denoting a reference refractive index, e.g. corresponding to freestream conditions. The optical wavefronts can be represented as isosurfaces of the OPL, i.e.,

$$\text{OPL}(\mathbf{x}, t) = \text{const.}, \quad (4)$$

as indicated schematically in figure 1. As long as the flow speeds are small relative to the speed of light, and the optical-beam propagation distances are small enough for light to propagate through the flow before it has evolved, it is sufficient to think of the OPL integral in equation 1 as involving only the instantaneous spatial structure of the refractive-index field, at each instant in time.

As the optical wavefronts propagate through the nonuniform refractive-index field  $n(\mathbf{x}, t)$ , the aerooptical interactions physically occur across the refractive fluid interfaces. These are the interfaces on which the refractive index  $n$  is constant. It is important to understand the role of these interfaces. While these fluid interfaces correspond to isosurfaces of the refractive-index field, i.e.,

$$n(\mathbf{x}, t) = \text{const.}, \quad (5)$$

it is crucial to recognize that the refractive-fluid interfaces will have a physical thickness whereas the refractive-fluid isosurfaces are geometrical objects with zero thickness. It is the physical thickness of the interfaces that is very important in aerooptics. We can introduce the local *interfacial fluid thickness*  $h_n$ , defined per unit  $n$ , as the inverse of the refractive-index gradient magnitude, i.e.,

$$h_n(\mathbf{x}, t) \equiv \frac{1}{|\nabla n|}. \quad (6)$$

The distance between two neighboring isosurfaces, corresponding to  $n$  and  $n + dn$ , will be  $h_n dn$ . This is shown schematically in figure 2, for a single interface, and in figure 3 for several neighboring interfaces. We can distinguish between the general case, where the gradient magnitude is nonzero, i.e.  $|\nabla n| > 0$ , and the special case of zero gradient magnitude, i.e.  $|\nabla n| = 0$ , which will be discussed below. In regions of relatively-large refractive-index gradients, the isosurfaces are closely spaced and the interfaces are associated with a relatively-small thickness. In regions of weak refractive-index gradients, the isosurfaces will be located further apart and the interfaces will be relatively thicker. The interfacial

fluid thickness can be expected to be highly nonuniform at large Reynolds numbers. This is because of the strongly-intermittent character of fully-developed turbulent flows which becomes more intermittent with increasing Reynolds number for both incompressible and compressible flows (e.g. Sreenivasan<sup>10</sup>, and references therein; Smits & Dussauge<sup>6</sup>). As discussed by Jumper & Fitzgerald<sup>1</sup>, refractive-index fluctuations can arise in pure fluids, e.g. where density fluctuations are induced by temperature variations in low-speed air flows (e.g. Jumper & Hugo<sup>11</sup>) or density fluctuations in compressible air flows (e.g. Fitzgerald & Jumper<sup>12</sup>), or in mixtures of dissimilar fluids (e.g. Brown & Roshko<sup>13</sup>; Dimotakis, Catrakis, & Fourguette<sup>5</sup>). In all these different cases, the thickness of the refractive interfaces can be defined in the same manner, i.e. using equation 6. We note that the present approach could be formulated entirely in terms of the refractive-index gradient. The interfacial fluid thickness, however, is especially helpful for physical insight into the aerooptical interactions.

Is the interfacial fluid thickness finite? Is it nonzero? In turbulent flows, the interfacial fluid thickness can be expected to be both nonzero and finite, in general, on physical grounds. The thickness must be nonzero wherever the local refractive-index gradient magnitude  $|\nabla n(\mathbf{x}, t)|$  is finite, as indicated from equation 6. Only an infinite gradient can lead to a zero interfacial fluid thickness. Physically, it is clear that for flows of real fluids, even at large but finite Reynolds numbers, the finite molecular diffusivities of the fluid ensure finite gradients and therefore finite interfacial fluid thicknesses. A related observation, also indicated from equation 6, is that the thickness must be finite as long as the gradient magnitude is nonzero. If the gradient is zero, which would correspond to a region of exactly-uniform refractive index, the thickness would be infinite in the context of equation 6 and one then must interpret the (infinity-times-zero) product  $h_n dn$  as a Dirac delta function whose integral becomes the distance given by the extent of the uniform-index region in the direction of the optical-ray propagation. In summary, we can expect physically that the interfacial fluid thickness must be finite as long as the gradient is finite, consistent with equation 6. The thickness is an interfacial property, therefore, that has to be taken into account.

Since each optical ray physically propagates through refractive interfaces, one can intuitively expect that the local interfacial fluid thickness should determine, at least in part, the local contribution to the OPL. Can this be seen directly in the OPL integral in equation 3? This can be done by rewriting equation 3, from the point of view of the refractive fluid

interfaces, as

$$\text{OPL}(\mathbf{x}, t) \equiv \int_{\text{ray}} n(\ell, t) h_{n,\ell} |\text{d}n|, \quad (7)$$

where the integration is now performed with respect to the refractive index  $n$ , rather than with respect to the spatial distance  $\ell$ , and  $h_{n,\ell}$  is the *effective interfacial fluid thickness* defined as the component of the interfacial thickness in the direction of optical propagation, given by

$$h_{n,\ell} = \frac{1}{|\nabla n|_\ell}, \quad (8)$$

with  $|\nabla n|_\ell$  denoting the effective gradient magnitude, i.e. the magnitude of the component of the local refractive-index gradient in the  $\ell$  direction, i.e. in the direction of the optical-ray propagation. The component of the refractive-index gradient in equation 7 is,

$$|\nabla n|_\ell \equiv \frac{|\text{d}n|}{\text{d}\ell}, \quad (9)$$

as required in order for equations 2 and 6 to be consistent. Since the refractive index  $n$  could be locally increasing or decreasing as the light rays propagate, it is necessary to express the differential of  $n$  as the absolute-valued differential  $|\text{d}n|$ , in equation 7. For interfaces locally normal to the optical rays, the gradient component  $|\nabla n|_\ell$  has magnitude identical to the magnitude of  $|\nabla n|$ . Where the interfaces are locally not perpendicular to the optical rays, this component will be of smaller magnitude than  $|\nabla n|$  and the effective interfacial fluid thickness will be larger. In other words, the effective gradient is always *less than or equal to* the full gradient, i.e.

$$|\nabla n|_\ell \equiv |\nabla n| |\cos \theta| \leq |\nabla n|, \quad (10)$$

and the effective interfacial fluid thickness is always *greater than or equal to* the full interfacial fluid thickness, i.e.

$$h_{n,\ell} = \frac{1}{|\nabla n|_\ell} \equiv h_n |\sec \theta| \geq h_n, \quad (11)$$

where the angle  $\theta$ , taken as  $-\pi < \theta \leq \pi$ , quantifies the interfacial orientation relative to the optical-propagation direction. These are important considerations as they can be used to develop a modeling approach based on the interfacial fluid thickness, described below in §4. As long as the refractive-index gradient magnitude is not zero, i.e. as long as  $|\nabla n| > 0$ , we can define  $\theta$  as the angle between the refractive-index gradient vector and the local optical-ray propagation vector. The refractive-index gradient vector is always normal to the

local refractive interface. Combining equations 11 and 7, and writing again equation 7 for clarity, we see that the OPL integral of equation 3 can be expressed directly in terms of the interfacial-fluid-thickness variations along the optical beampropagation path as,

$$\text{OPL}(\mathbf{x}, t) \equiv \int_{\text{ray}} n(\ell, t) h_n |\sec \theta| |dn| = \int_{\text{ray}}^{\perp} n(\ell, t) h_{n,\ell} |dn|, \quad (12)$$

where the first integral is in terms of the thickness  $h_n$  and relative orientation  $\theta$  of the refractive interfaces, and the second integral is in terms of the effective interfacial fluid thickness  $h_{n,\ell}$ . As mentioned above, in the context of the interfacial fluid thickness in equation 5, these integrals require that  $|\nabla n| \neq 0$ . In those regions where  $|\nabla n| = 0$ , i.e. in regions of uniform refractive index, the (infinity-time-zero) product  $h_n dn$  must be interpreted again as a Dirac delta function whose integral is the distance, say  $\Delta\ell$ , corresponding to the extent of the uniform-index region in the optical-propagation direction, so that the contribution to the OPL integral becomes  $\Delta(\text{OPL}) = n \Delta\ell$ . We note that, in uniform-index regions, the interfacial orientation  $\theta$  has no meaning and is not needed. In those instances where the fluid interface happens to be locally tangent to the optical-propagation direction, i.e. if  $\theta = \pm \pi/2$ , the term  $|\sec \theta|$  will be infinite but in such cases the refractive index will locally be uniform since the interface will be aligned with the optical-propagation direction, i.e.  $|dn| = 0$  in such cases. In those cases, therefore, the contribution to the OPL integral will again be  $\Delta(\text{OPL}) = n \Delta\ell$  with  $\Delta\ell$  identified as the length of the interface that is tangential to the optical-propagation direction. We should also note that, in general, one may also need to take into account other possibilities such as total internal reflection or the development of caustics. These possibilities depend on the magnitudes of refractive gradients, and relative interfacial orientations, encountered in practice.

In summary, the proposed interfacial-fluid-thickness approach is based on relating the OPL to the interfacial-fluid-thickness variations. Whereas the integral in equation 3 is conducted over space, the integrals in equations 7 and 12 are expressed as integrals over the refractive index and are useful to determine the manner in which the refractive interfaces physically contribute to the OPL. In addition to the local refractive index  $n$ , equation 11 shows that the OPL variations arise from the variability in the interfacial fluid thickness  $h_n$  and the fluctuations in the interfacial orientation  $\theta$ , or the variations in the effective interfacial fluid thickness  $h_{n,\ell}$ . Knowledge of the variability in the effective interfacial fluid

thickness, and its relation to the flow dynamics, can be expected therefore to provide physical insight into the relation between the OPL behavior and the interfacial structure.

### 3. Demonstration on high-compressibility turbulent-shear-layer fluid interfaces

In this section, we demonstrate the use of the interfacial-fluid-thickness approach on turbulent high-compressibility fluid interfaces. We have chosen to examine the applicability of the proposed approach to high-compressibility fluid interfaces in order to develop a large-scale aerooptics modeling methodology useful for high-compressibility flow conditions. This will be described in the next section (§4). There are available large-scale aerooptics modeling methods that have successfully addressed weakly-compressible flows (e.g. Jumper & Fitzgerald<sup>1</sup>) and incompressible flows (e.g. Truman & Lee<sup>3</sup>; Chew & Christiansen<sup>14</sup>; Dimotakis, Catrakis, & Fourguette<sup>5</sup>). These methods are based essentially on the Brown-Roshko large-scale organized-structure approach (Brown & Roshko<sup>13</sup>) with direct extensions to weakly-compressible flows, and will be discussed briefly in §4. It is known, however, that high-compressibility turbulent flows exhibit significant differences compared to weakly-compressible or incompressible flows (e.g. Papamoschou & Roshko<sup>15</sup>; Papamoschou 1991<sup>16</sup>; Clemens & Mungal<sup>17</sup>). A more general approach is desirable, to be able to address aero-optical effects across the full range of compressibilities, and it is toward this goal that the interfacial-fluid-thickness approach of §2 can be particularly useful.

Figure 4a shows an example of a two-dimensional spatial streamwise slice of the refractive-index field in a shear layer between optically-different gases, with convective Mach number  $M_c \sim 1$  and Reynolds number  $Re \sim 10^6$  based on the large-scale extent  $L_\delta$  of the flow (Dimotakis, Catrakis, & Fourguette<sup>5</sup>). Also shown is an example of a low-compressibility ( $M_c \sim 0.2$ ) shear-layer image in figure 4b, for comparison. These flow images span the entire large-scale transverse extent of the flow and, although not fully resolved, they capture a relatively-wide range of scales ( $\sim 500 : 1$ ) which permits a study of the large-scale behavior. The imaging technique relies on Rayleigh scattering and on using dissimilar gases that have a large difference in scattering cross section and a relatively large difference in refractive index. The low-speed freestream contains ethylene in both the high- and low-compressibility cases, while the high-speed freestream contains helium or nitrogen for the high- or low-compressibility cases respectively. The freestream refractive-index difference is  $\Delta n \sim 6.6 \times 10^{-4}$  or  $\Delta n \sim 4.0 \times 10^{-4}$ , for the high- or low-compressibility cases respectively, at the flow

conditions investigated. A pulsed laser at a visible wavelength of 532 nm and with energy of  $\sim 300$  mJ per pulse provided the illumination source for the flow imaging. A description of the flow facility and further details of the experimental technique can be found in Dimotakis, Catrakis, & Fourguette.<sup>5</sup>

It should be noted that the refractive-index field in figure 4a reflects effects of both mixing and compressibility, as a result of the use of optically-different gases, and may not directly represent the density-field behavior, as has been discussed by Jumper & Fitzgerald.<sup>1</sup> The issue of the relative effects of mixing vs. density variations is important. It is helpful to appreciate first that nearly-uniform concentration regions, in the case of mixing, are consistent with and directly related to low-density wells corresponding to concentrated-vorticity structures, e.g. organized vortical structures. In fact the presence of nearly-uniform regions in the case of mixing provides indirect evidence of these low-density wells. The density-well approach of Jumper & Fitzgerald<sup>1</sup> and the uniformly-mixed-region approach of Dimotakis, Catrakis, & Fourguette<sup>5</sup> are both related to the original Brown-Roshko<sup>13</sup> organized-structures approach since the Brown-Roshko structures, originally recorded at incompressible conditions, are the dominant large-scale vortical structures at low or no compressibility. It is of course also important to remember that the density wells become deeper as the level of compressibility rises. Although the underlying fluid mechanics is the same, i.e. the same vortical structures generate the low-density wells and the uniformly-mixed regions, the magnitude of the aerooptical effects associated with mixing effects vs. pure density effects can be expected to be quite different. It is clear that the difference between these two effects, aerooptically, can be large depending on the choice of the dissimilar gases as opposed to the pure-air total-temperature-matched freestreams. Two types of aerooptical applications, for example, where mixing effects can be important are high-speed-flow applications, where a film coolant may need to be injected near the optical window and this would generate mixing between the coolant and the air, i.e. between the dissimilar gases, and possible future aerooptics applications whereby one may need to be able to vary or optimize the level of optical distortions across a wide range of magnitudes.

The primary emphasis of the present work is on the interfacial-fluid-thickness approach, which is a general approach and can be expected to be useful for studying both mixing and density effects in the future. The data used presently to demonstrate this approach

are dominated by the mixing effect but, again, the main approach described in §2 is of general use, i.e. it is not restricted to either effect. The data in figure 4a make possible an examination of the interfacial-fluid-thickness approach at high levels of compressibility even though the density-field variations associated with the mixing field, can be expected to exhibit features attributable to not only vortical structures, but also compression-wave regions (e.g. shocklets) and expansion-wave regions. The refractive-index field in figure 4a reflects these flow mechanisms, albeit indirectly, and provides the opportunity to examine the role of high-compressibility fluid interfaces and in particular their physical thickness in generating the aerooptical distortions.

The interfacial-fluid-thickness fields,  $h_n$ , corresponding to the refractive-index fields,  $n$  of figures 4a and b, are shown in figures 5a and b. The IFT was computed by first evaluating the refractive-index gradient magnitude  $|\nabla n|$  and subsequently computing its inverse (Aguirre, Ruiz-Plancarte, & Catrakis<sup>18</sup>), according to the IFT definition in equation 6 of §2. The local refractive-gradient magnitudes, and interfacial fluid thicknesses, are necessarily under-/over-estimated respectively because the images are not fully resolved. The computed gradients and thicknesses are essentially coarse-grained values at the image-resolution scale. However, these values permit the *relative spatial variations* to be examined and this is what is needed in the present context. Since the refractive-index data of figures 5a and b are from two-dimensional slices of the flow, only two of the three spatial refractive-index derivatives necessary to evaluate the full gradient magnitude can be computed. The IFT fields in figures 5a and b thus correspond to the in-plane refractive-index gradient magnitude. We note, however, that only the component of the full gradient, or interfacial fluid thickness, along the optical-ray propagation direction is needed, as is evident in equations 9, 10, and 11 in §2. In other words, even if the full gradient were available, one would compute the component of it in the optical-propagation direction and this would be equivalent to using the in-plane component in addition to the in-plane interfacial orientation, for optical wavefronts propagating in the plane of the flow shown in figures 5a and b, or figures 4a and b. In figures 5a and b, the in-plane gradient magnitudes are shown such that darker regions denote higher values of the gradient magnitude. Since the in-plane interfacial fluid thickness is the inverse of the in-plane gradient magnitude, the darker regions denote locally-thin high-gradient interfaces. Also evident in figures 5a and b are the variations in the interfacial orientation. Depending on the direction of optical beam propagation, the relative interfacial orientation  $\theta$  will be

different along the beam-propagation path. Figures 5a and b indicate, however, that the interfacial orientation is sufficiently irregular that, at least locally, there is a wide distribution of interfacial directions. It is important to recall the meaning of equations 10 and 11 from §2, i.e. that interfaces of a given thickness will have an effective thickness that is always greater than or equal to it for any optical-beam propagation direction. In other words, a given gradient magnitude will result in an effective gradient magnitude that is always smaller than or equal to it, irrespective of the optical-beam propagation direction. If one identifies, therefore, the regions of high-gradient interfaces in the flow, then there can be no effective gradient magnitudes that are higher yet.

Four significant observations can be made, at high compressibility, on the basis of figure 5a and other interfacial-fluid-thickness fields at the same flow conditions:

- (a) *the high-gradient regions occupy a relatively-small part of the turbulent shear-flow region,*
- (b) *the high-gradient regions are sheet-like and can be thought of as high-gradient interfaces,*
- (c) *the high-gradient interfaces exist at various transverse locations in the shear-flow region, and*
- (d) *the refractive-index gradient magnitude exhibits variations along the high-gradient interfaces.*

It is important to note that these observations refer to the *instantaneous* spatial structure of the interfacial-fluid-thickness field, and this is practically what is most relevant for aerodynamics since it is the instantaneous flow structure that needs to be understood, modeled, and controlled. The ensemble-averaged behavior can be expected of course to be quite different and simpler with smooth ensemble-averaged interfaces.

Observation (a) refers to the fact that the high-gradient regions are spatially relatively isolated, as is evident in figure 5a. In other words, *large parts of the instantaneous flow region have relatively low refractive-gradient magnitudes.* The high-gradient regions appear to occupy only a small fraction of the flow region. This is consistent with computational results at low Reynolds numbers in studies by Samtaney, Pullin, & Kosović<sup>19</sup> who found

that regions of high gradient magnitudes in isotropic and homogeneous turbulence occupy a relatively-small fraction of the flow.

Observation (b) indicates, further, that the high-gradient regions are not only spatially isolated but are sheet-like, i.e. these regions are confined to thin layers in the turbulent-flow region. These high-gradient regions can be thought of physically, therefore, as *locally-thin interfaces*. Sheet-like structure, in three-dimensional space, is consistent with the string-like structure evident in the two-dimensional spatial images or slices such as figure 5a.

Observation (c) is particularly important because it illustrates a major qualitative difference between high-compressibility flows and weakly-compressible flows. The data indicate that the high-gradient interfaces, although spatially isolated and occupying a relatively small fraction of the flow region, are present at *several different transverse locations in the instantaneous flow structure*, as is evident in the high-compressibility interfacial-fluid-thickness field of figure 5a and in direct contrast to the low-compressibility interfacial-fluid-thickness field of figure 5b. Whereas at low compressibility, the high-gradient interfaces are mostly confined to the instantaneous outer edges of the flow, it is clear that at high compressibility the high-gradient interfaces can be found both in the interior and near the outer boundaries in instantaneous realizations of the flow. This is in sharp contrast with the behavior in low-compressibility turbulent shear flows (Truman & Lee<sup>3</sup>; Dimotakis, Catrakis, & Fourguette<sup>5</sup>), cf. the interfacial-fluid-thickness behavior in figure 5b, where isolated high-gradient regions are not found in the interior of the flow, as a result of large-scale organized structures which confine such interfaces mostly to the outer parts of the shear region. At the high-compressibility flow conditions examined presently in figure 5a, the high-gradient interfaces are clearly not confined to the outer boundaries of the flow and are not excluded from the interior of the flow.

Observation (d) is also important because it indicates that, on the high-gradient interfaces, the refractive-index gradient is not constant, i.e. it fluctuates along these interfaces. This must be taken into account if one wishes to model the aerooptical effects of these interfaces, and this will be addressed in the proposed modeling approach in §4 below. We note that the variability of the thickness along the high-gradient interfaces is attributable to both intermittency effects associated with the large Reynolds number and the presence of compact shocklets associated with the high compressibility of the flow.

These observations, and the dramatic difference between the high-compressibility behavior and the low-compressibility behavior, are illustrated also in figures 6a and b. The observation, at high compressibility, that the high-gradient regions are spatially isolated even though they occupy several transverse locations in the flow, and the interpretation of the optical wavefront phase in terms of the interfacial fluid thickness variations (cf. §2), indicate that these isolated regions are the dominant elements for the large-scale optical distortions at high compressibility. While the low-gradient regions are of wide transverse extent, and therefore do contribute to the OPL integral, it is the structure of the high-gradient (locally-thin) interfaces that can form the basis of a description that captures the large-scale optical distortions, as explained in the modeling approach proposed in the following section.

#### 4. Proposed large-scale aerooptics modeling approach based on high-gradient interfaces

The observations of the instantaneous structure of the interfacial-fluid-thickness field, in §3, and the interpretation of the OPL in terms of the interfacial-fluid-thickness variations, in §2, can be used to develop a modeling methodology that is useful for capturing the large-scale optical distortions at high compressibility. Before describing the proposed modeling approach, it is helpful to recall the previous work in incompressible and weakly-compressible shear layers that has been successful in modeling the large-scale aerooptical distortions. In the case of incompressible shear layers of dissimilar gases, the Brown-Roshko vortical structures (Brown & Roshko<sup>13</sup>) generate large-scale regions of nearly-uniform refractive index and this enables the use of the outer interfaces to model the large-scale optical distortions (Dimotakis, Catrakis, & Fourguette<sup>5</sup>). We note, however, that the 'outer-interface' model of Dimotakis, Catrakis, & Fourguette<sup>5</sup> is only applicable to mixing cases, i.e. it does not address the density effects. In the case of weakly-compressible shear layers, there are large-scale regions of reduced density and pressure in the flow as shown by Fitzgerald & Jumper.<sup>12</sup> These large-scale reduced-density regions are essentially weakly-compressible analogues of the Brown-Roshko structures. Jumper & Fitzgerald<sup>1</sup> have developed a model based on these large-scale low-density regions, or density wells, and have shown that it is able to reproduce well the large-scale optical distortions at low compressibility. The present IFT framework (§2) is a general approach and thus is not restricted to low compressibilities.

It is known, from various investigations of high-compressibility flows, that there is a

strong qualitative difference between the structure of weakly-compressible flows and high-compressibility flows (e.g. Bogdanoff<sup>20</sup>; Papamoschou & Roshko<sup>15</sup>; Papamoschou<sup>16</sup>; Samimy & Elliott<sup>21</sup>; Samimy, Reeder, & Elliott<sup>22</sup>; Clemens & Mungal<sup>17</sup>). For shear layers, in addition to the well-known reduction in the growth rate there is a substantial difference in the organization of the flow and in particular in the internal structure of the flow as the compressibility level is increased. In particular, accepting the convective Mach number  $M_c$  as an adequate measure of compressibility,

$$M_c \equiv \frac{U_1 - U_2}{a_1 + a_2}, \quad (13)$$

where  $U_{1,2}$  and  $a_{1,2}$  denote the freestream speeds and sound speeds, respectively, there is evidence that the flow behavior transitions and changes significantly at convective Mach numbers above a certain value (Clemens & Mungal<sup>17</sup>). Specifically, in the range

$$M_c \gtrsim 0.6, \quad (14)$$

which corresponds to high compressibility according to most available data, the turbulent flow structure and fluid interfaces appear to be substantially more irregular, and in a fundamentally-different way, compared to the behavior at low compressibility.

Comparison of the images in figures 5a and b, example, indicates that high-compressibility shear layers exhibit *multiple* regions spanning different transverse locations where the refractive-index gradients are relatively weak. At the boundaries between these multiple regions, the high-gradient interfaces reside. As discussed in §3, these high-gradient interfaces appear to form a highly-irregular network in the flow. Is there a way to model the interfacial-fluid-thickness field at high compressibility in order to reproduce the aerooptical distortions? In particular, how can the large-scale optical distortions be modeled at high compressibility and which part of the interfacial-fluid-thickness structure is necessary to capture the large-scale optical distortions?

Our proposed modeling approach, at high compressibility, is based on the crucial observation in §3 that the high-gradient interfaces, although located at various transverse locations, are *spatially isolated*, cf. figures 5a and 6a. Because the high-gradient interfaces occupy a relatively-small fraction of the total turbulent-flow region, we can develop a modeling approach with these interfaces as the dominant elements. A gradient-magnitude threshold is first chosen in order to identify the high-gradient interfaces. We note that it is crucial to

retain the high-gradient interfaces. It may appear, at first sight, that these high-gradient interfaces could be neglected since they only occupy a small fraction of the turbulent-flow region. On the contrary, the high-gradient interfaces contribute significantly to the OPL integral because, even though the thickness  $h_{n,l}$  is relatively small, the differential  $|dn|$  is relatively large across such interfaces. Significantly, there is no way to avoid including these high-gradient interfaces in the modeling approach. Fortunately, however, it is precisely because these interfaces are spatially isolated that it is feasible to approximate the regions in between these interfaces as zero-gradient regions, i.e. as uniform-index regions. This raises the important question of how to propagate the beam, in the model, through these regions. For comparison, in the Dimotakis, Catrakis, & Fourguette<sup>5</sup> modeling approach, the refractive index in the large-scale regions bounded by the outer interfaces is modeled on the basis of the value predicted from the large-scale entrainment. For the present case of high compressibility, however, there are multiple regions through which the beam must be propagated. We propose that the way to do this is to use the *gradient information* along the high-gradient interfaces to update the refractive index as the OPL integral is computed across these interfaces. The *locations* of the high-gradient interfaces provide the length scales needed to propagate the beam through the regions in between the interfaces. The proposed modeling approach can be summarized therefore in four steps:

- (a) *the high-gradient interfaces are first identified, including their spatial location and gradient values,*
- (b) *the optical beam is propagated across the high-gradient interfaces by updating the OPL integral using the gradient values at these interfaces,*
- (c) *the regions in between the high-gradient interfaces are modeled as zero-gradient regions, and,*
- (d) *the value of the refractive index in each zero-gradient region, between the high-gradient interfaces, is computed using the gradient value on the interface which the beam propagates across as it enters each zero-gradient region.*

A schematic illustrating the basic idea of this model is shown in figure 7 for the high-compressibility case. The multiple regions in the interior of the flow are denoted as  $B$

through  $G$ . We emphasize that it is important, and necessary, to retain both the *location of* and *gradient values along* the high-gradient interfaces in the proposed modeling approach.

The utility of this approach can be demonstrated with the high-compressibility IFT data examined in §3. Figure 8 shows a modeled interfacial-fluid-thickness field where  $\sim 50\%$  of the refractive-gradient magnitudes have been set to zero, compared to the original field in figure 5a. The OPL integral was computed using this modeled IFT field by following the above four steps. The comparison between the full aerooptical-wavefront OPL (solid curve) and the modeled OPL (dashed curve) is shown in figure 9. Good agreement is evident in terms of the large-scale OPL variations. Different thresholds were examined spanning almost the entire range, i.e. from almost 100% to almost 0%. As expected, the ability of the thresholded field to capture the large-scale wavefront distortions was found to decrease with decreasing threshold. The important finding is that with modest threshold levels one can capture the large-scale wavefront signature. The 50% threshold employed in figure 8 was chosen as an example to illustrate that the high-gradient interfaces contain the essential information to model the large-scale optical distortions.

Figure 9 indicates that the proposed modeling approach can be used to reproduce the large-scale optical distortions at high compressibility, in a shear layer, using the high-gradient information. High-gradient interfaces both in the interior and near the outer boundaries of the flow are essential to capture the large-scale wavefront distortion. However, instead of the full interfacial-fluid-thickness field, information on the high-gradient interfaces only appears to be sufficient to model the large-scale aerooptical distortions. The location of the high-gradient interfaces and the value of the gradient across (or of the thickness of) these interfaces is enough to capture the dominant contributions that generate the large-scale aerooptical distortions. The optical wavefronts are propagated through the high-gradient (locally-thin) interfaces and the gradient value across these interfaces is used to compute the difference in the optical path length, while in the low-gradient regions between the high-gradient interfaces the wavefronts are propagated neglecting the presence of the low gradients, i.e. as if those regions are zero-gradient regions. The high-gradient interfaces, in this example, are identified in an absolute sense, i.e. by thresholding the entire instantaneous gradient field. A further refinement, potentially, could be envisaged by retaining those interfaces that have high gradients *relative to* their neighboring interfaces. The proposed

modeling approach offers a reduction in the amount of flow information needed to capture the large-scale aerooptical distortions at high compressibility.

## 5. Conclusions and implications

A new interfacial-fluid-thickness (IFT) approach is proposed to examine optical-wavefront propagation through turbulent flows in terms of the variability in the physical thickness of the refractive fluid interfaces. The interfacial fluid thickness is given by the inverse of the refractive-index gradient magnitude, and it is highly variable at large Reynolds numbers and high compressibility. The IFT plays an important role in aerooptics as indicated by expressing directly the optical path length (OPL) in terms of the interfacial-fluid-thickness variations. Demonstration of this approach on refractive-field data in shear layers at high compressibility ( $M_c \sim 1$ ) and large Reynolds number ( $Re \sim 10^6$ ) reveals that regions of high refractive-gradient magnitudes are located at various transverse locations in the flow, i.e. both in the interior and near the outer boundaries, and form highly-irregular networks. Significantly, the high-gradient regions are found to be spatially isolated, i.e. occupy a relatively-small fraction of the shear layer. This observation, coupled with the interpretation of the OPL in terms of interfacial-fluid-thickness variations, are utilized to propose and demonstrate a new modeling approach where the high-gradient interfaces are the dominant elements necessary to reproduce the large-scale optical distortions at high compressibility. Both the location of and the gradient values along the high-gradient interfaces are utilized in this modeling approach. As an example, a reduction of  $\sim 50\%$  in the amount of interfacial information needed is shown to reproduce well the large-scale optical distortions at high compressibility. The present results suggest applicability of the proposed approach to other high-compressibility flows, by modeling the large-scale optical distortions in terms of the structure of the high-gradient interfaces. The proposed approach can be expected to be useful in studies of the dynamics of aerooptical interactions at high compressibility (e.g. Thurow, Samimy, Lempert, Harris, Widiker, & Duncan<sup>23</sup>), in computational modeling and simulations of aerooptical interactions in high-speed flows (e.g. Jones & Bender<sup>24</sup>), as well as in efforts to extend fluid-mechanical techniques that control or regularize aerooptical interactions in weakly-compressible flows (e.g. Stanek, Sinha, Seiner, Pearce, & Jones<sup>25</sup>), Siegenthaler, Jumper, & Asghar<sup>26</sup>) to higher flow compressibilities.

## Acknowledgements

This work is supported by the Air Force Office of Scientific Research through Grants F49620-02-1-0142 and F49620-02-1-0277 (Dr. T. Beutner, Program Manager) and is part of a program on aero-optical interactions in turbulent flows. The authors are grateful to Col. Dr. Demos Kyrazis and Prof. Eric Jumper for their valuable advice, to Prof. Ronald Hugo, Dr. Edward Fitzgerald, Dr. Michael Jones, and Prof. Randall Truman for helpful discussions, and to the Reviewers for their insightful comments. Earlier ideas of the authors that led to the development of the interfacial-fluid-thickness approach were presented as AIAA Paper 2002-2269 in Maui, Hawaii, and AIAA Paper 2003-0642 in Reno, Nevada.

## References

- <sup>1</sup>Jumper, E. J. and Fitzgerald, E. J., "Recent advances in aero-optics," *Prog. Aerospace Sci.*, Vol. 37, 2001, pp. 299–339.
- <sup>2</sup>Gilbert, K. G. and Otten, L. J., "Aero-optical phenomena," *Progress in Astronautics and Aeronautics*, Vol. 80, American Institute of Aeronautics and Astronautics, 1982.
- <sup>3</sup>Truman, C. R. and Lee, M. J., "Effects of organized turbulence structures on the phase distortion in a coherent optical beam propagating through a turbulent shear flow," *Phys. Fluids A*, Vol. 2, 1990, pp. 851–857.
- <sup>4</sup>Wissler, J. B. and Roshko, A., "Transmission of thin light beams through turbulent mixing layers," *AIAA 30<sup>th</sup> Aerospace Sciences Meeting*, AIAA-92-0658, Reno, NV, 1992.
- <sup>5</sup>Dimotakis, P. E., Catrakis, H. J., and Fourguette, D. C. L., "Flow structure and optical beam propagation in high-Reynolds-number gas-phase shear layers and jets," *J. Fluid Mech.*, Vol. 433, 2001, pp. 105–134.
- <sup>6</sup>Smits, A. J. and Dussauge, J.-P., *Turbulent Shear Layers in Supersonic Flow*, AIP Press, 1996.
- <sup>7</sup>Catrakis, H. J., Aguirre, R. C., and Nathman, J. C., "Aero-optical wavefront scale-local structure in large-Reynolds-number compressible turbulence," *AIAA J.*, 2004, forthcoming.
- <sup>8</sup>Liepmann, H. W., "Deflection and diffusion of a light ray passing through a boundary layer," Douglas Aircraft Company Report SM-14397, Santa Monica, CA.
- <sup>9</sup>Liepmann, H. W., "Aspects of the Turbulence Problem. Part 2: IV. General discussion, V. Isotropic Turbulence," *Z. angew. Math. Phys.*, Vol. 3, 1952, pp. 407–426.
- <sup>10</sup>Sreenivasan, K. R., "Fractals and multifractals in fluid turbulence," *Annu. Rev. Fluid. Mech.*, Vol. 23, 1991, pp. 539–600.

<sup>11</sup>Jumper, E. J. and Hugo, R. J., "Quantification of aero-optical phase distortion using the small-aperture beam technique," *AIAA J.*, Vol. 33, 1995, pp. 2151–2157.

<sup>12</sup>Fitzgerald, E. J. and Jumper, E. J., "Scaling aero-optic aberrations due to propagation through compressible shear layers," *AIAA 2000-2354*, 2000.

<sup>13</sup>Brown, G. L. and Roshko, A., "On density effects and large scale structure in turbulent mixing layers," *J. Fluid Mech.*, Vol. 64, 1974, pp. 775–816.

<sup>14</sup>Chew, L. and Christiansen, W., "Coherent structure effects on optical performance of plane shear layers," *AIAA J.*, Vol. 29, 1991, pp. 76–80.

<sup>15</sup>Papamoschou, D. and A., R., "The compressible turbulent shear layer: an experimental study," *J. Fluid Mech.*, Vol. 197, 1988, pp. 453–477.

<sup>16</sup>Papamoschou, D., "Structure of the compressible turbulent shear layer," *AIAA J.*, Vol. 29, 1991, pp. 680–681.

<sup>17</sup>Clemens, N. T. and Mungal, M. G., "Large-scale structure and entrainment in the supersonic mixing layer," *J. Fluid Mech.*, Vol. 284, 1995, pp. 171–216.

<sup>18</sup>Aguirre, R. C., Ruiz-Plancarte, J., and Catrakis, H. J., "Physical thickness of turbulent fluid interfaces: structure, variability, and applications to aero optics," *AIAA 41<sup>st</sup> Aerospace Sciences Meeting and Exhibit, AIAA 2003-0642*, Reno, Nevada, 2003.

<sup>19</sup>Samtaney, R., Pullin, D. I., and Kosović, B., "Direct numerical simulation of decaying compressible turbulence and shocklet statistics," *Phys. Fluids*, Vol. 13, 2001, pp. 1415–1430.

<sup>20</sup>Bogdanoff, D., "Compressibility effects in turbulent shear layers," *AIAA J.*, Vol. 21, 1983, pp. 926–927.

<sup>21</sup>Samimy, M. and Elliot, G. S., "Effects of compressibility on the characteristics of free shear layers," *AIAA J.*, Vol. 28, 1990, pp. 439–445.

<sup>22</sup>Samimy, M., Reeder, M. F., and Elliot, G. S., "Compressibility effects on large structures in free shear flows," *Phys. Fluids*, Vol. 4, 1992, pp. 1251–1258.

<sup>23</sup>Thurow, B., Samimy, M., Lempert, W., Harris, S. R., Widiker, J., and Duncan, B., "Simultaneous MHz rate flow visualization and wavefront sensing for aero optics," *AIAA 41<sup>st</sup> Aerospace Sciences Meeting & Exhibit, AIAA 2003-0684*, Reno, NV, 2003.

<sup>24</sup>Jones, M. and Bender, E. E., "CFD-based computer simulation of optical turbulence through aircraft flowfields and wakes," *AIAA 32<sup>nd</sup> Plasmadynamics and Lasers Conference, AIAA 2001-2798*, Anaheim, CA, 2002.

<sup>25</sup>Stanek, M., Sinha, N., Seiner, J., Pearce, B., and Jones, M., "Applying very high frequency excitation to the problem of tactical directed energy beam propagation," *AIAA 33<sup>rd</sup> Plasmadynamics and Lasers Conference, AIAA 2002-2272*, Maui, HI, 2002.

<sup>26</sup>Siegenthaler, J. P., Jumper, E. J., and Asghar, A., "A preliminary study in regularizing the coherent structures in a planar, weakly-compressible, free shear layer," *AIAA 41<sup>st</sup> Aerospace Sciences Meeting & Exhibit, AIAA 2003-0680*, Reno, NV, 2003.

*AIAA Journal*, Catrakis & Aguirre, Figure Captions

Figure 1. Schematic of a refractive-index field  $n(x, y; z, t)$  at high compressibility, shown as the gray-level image at the inset, with flow from left to right. Also shown is a planar incident optical wavefront (top), propagating from top to bottom, and a propagated distorted optical wavefront (bottom).  $L_\delta$  is the large-scale transverse extent of the flow and measures the extent of the outermost edges of the turbulent refractive fluid interfaces.

Figure 2. Schematic representation of a refractive interface, its interfacial fluid thickness  $h_n(\mathbf{x}, t)$ , and two neighboring isosurfaces of the refractive-index field  $n(\mathbf{x}, t)$ .

Figure 3. Schematic of several refractive fluid interfaces and the variability in interfacial fluid thickness.

Figures 4a and b. (a) Refractive-index field in a streamwise slice of a high-compressibility ( $M_c \sim 1$ ) large-Reynolds-number ( $Re \sim 10^6$ ) shear layer between optically-different gases.<sup>5</sup> (b) Low-compressibility ( $M_c \sim 0.2$ ) shear-layer refractive field.<sup>5</sup>

Figures 5a and b. (a) Interfacial-fluid-thickness field  $h_n$  at high compressibility corresponding to the refractive-index field of figure 4. Darker regions denote thinner interfaces, i.e. the dark regions correspond to the high-gradient interfaces. (b) Low-compressibility interfacial-fluid-thickness field.

Figure 6a and b. (a) Schematic of network of spatially-isolated high-gradient interfaces at high compressibility. Darker regions denote higher gradients or locally-thinner interfaces. (b) Schematic of high-gradient interfaces at low compressibility.

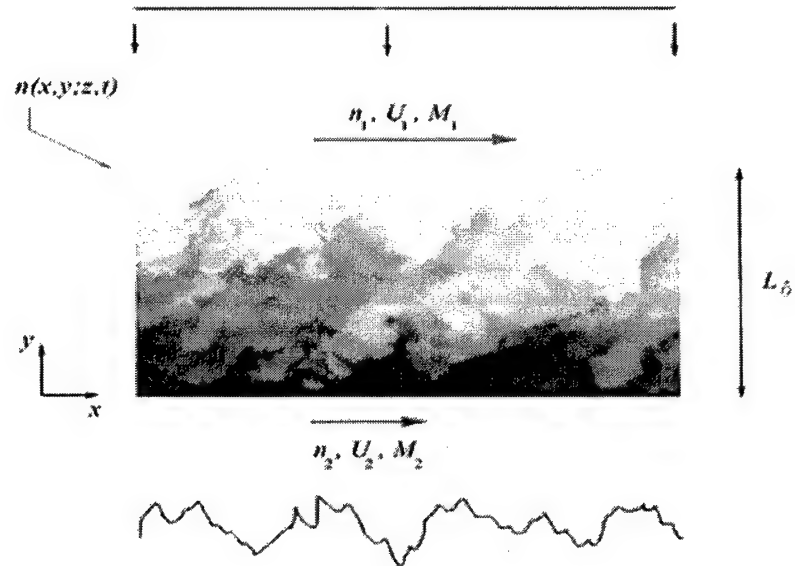
Figure 7. The labeled regions in the interior of the flow, i.e. regions  $B$  through  $G$ , correspond to the low-gradient regions at high compressibility. In the proposed modeling approach, the high-gradient interfaces, or boundaries between the low-gradient regions, are treated as the dominant elements necessary to model the large-scale optical distortions at high compressibility.

Figure 8. Modeled interfacial-fluid-thickness field, with  $\sim 50\%$  of the gradient magnitudes neglected, at high compressibility, cf. figure 5a.

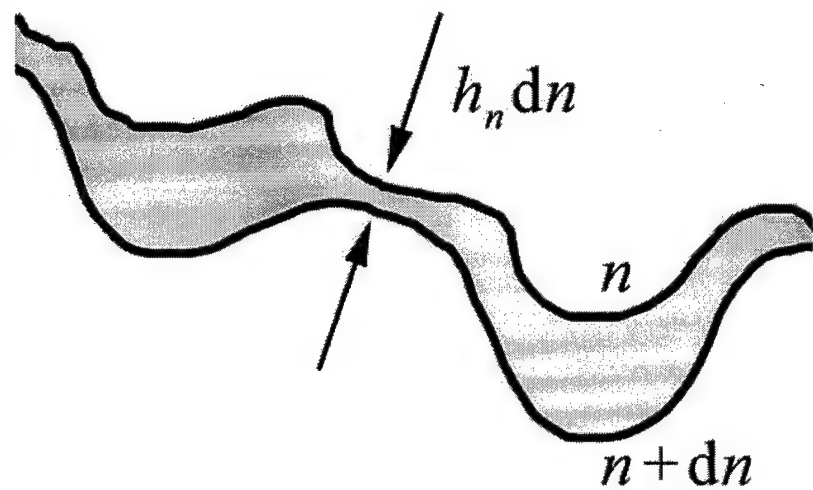
Figure 9. Comparison of the wavefront OPD, at high compressibility, between the full

wavefront OPD (solid curve) using the complete interfacial-fluid-thickness field (figure 5a), and the modeled OPD (dashed curve) using the high-gradient interfaces with  $\sim 50\%$  of the gradient magnitudes neglected (figure 8). The spatial and OPD coordinates are normalized based on the large-scale flow extent  $L_\delta$ , in a similar manner as in Dimotakis, Catrakis, & Fourguette<sup>5</sup>. The large-scale optical distortions, at high compressibility, can be captured in terms of the high-gradient interfaces only, even with a  $\sim 50\%$  reduction in interfacial information, demonstrating the utility of the proposed IFT modeling approach.

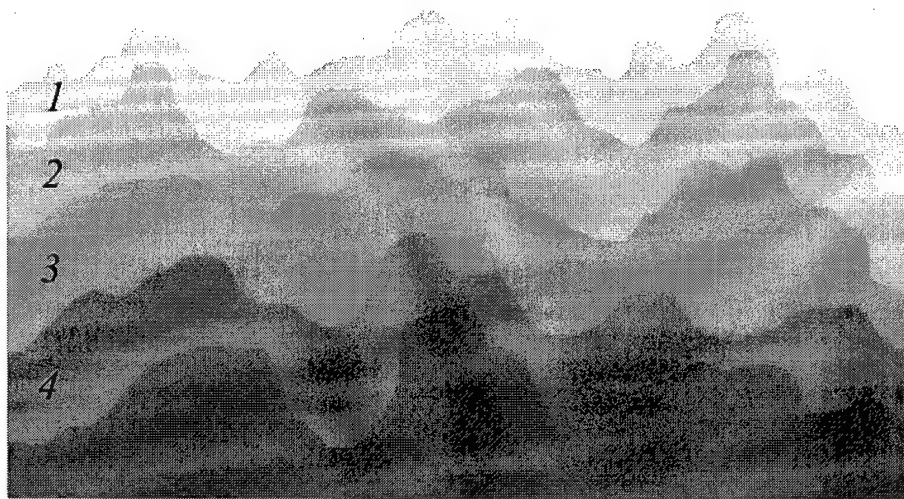
AIAA Journal, Catrakis & Aguirre, Figure 1



*AIAA Journal*, Catrakis & Aguirre, Figure 2



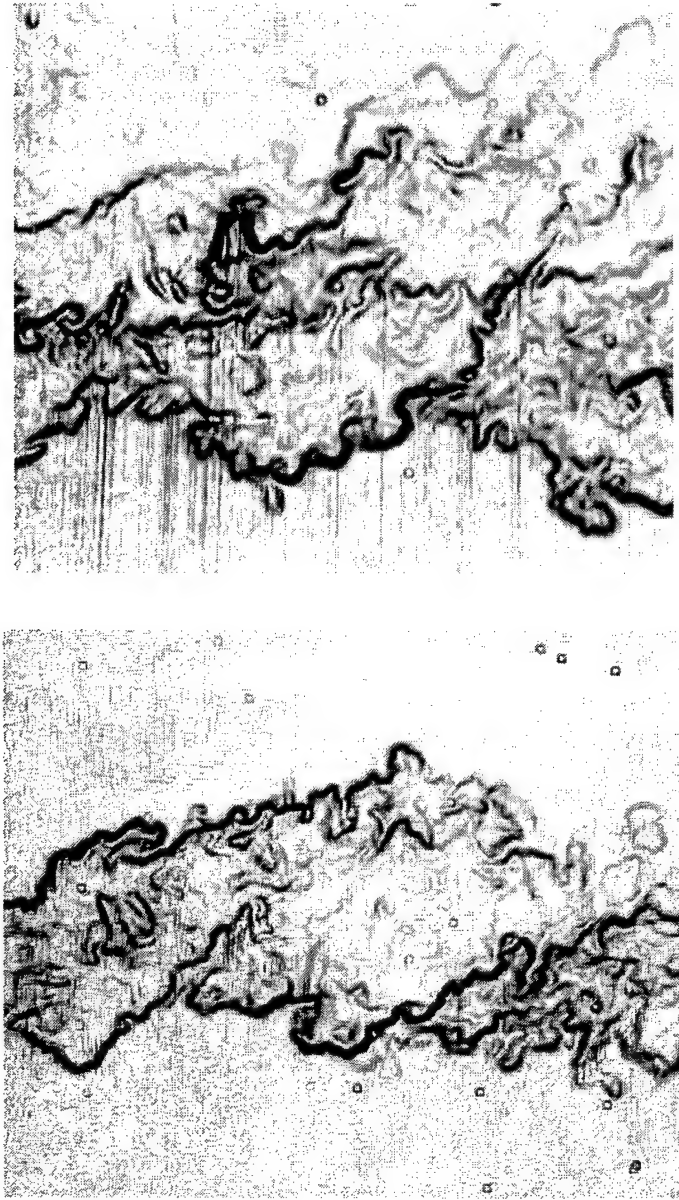
*AIAA Journal*, Catrakis & Aguirre, Figure 3



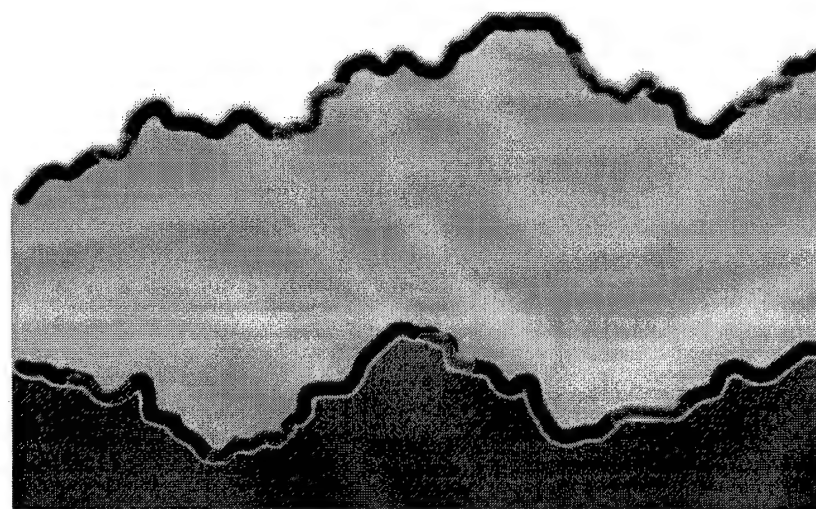
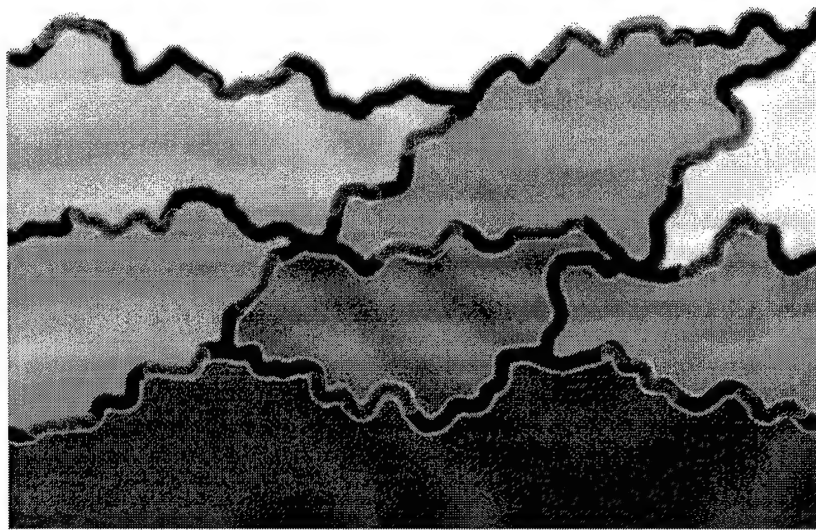
*AIAA Journal*, Catrakis & Aguirre, Figures 4a and b



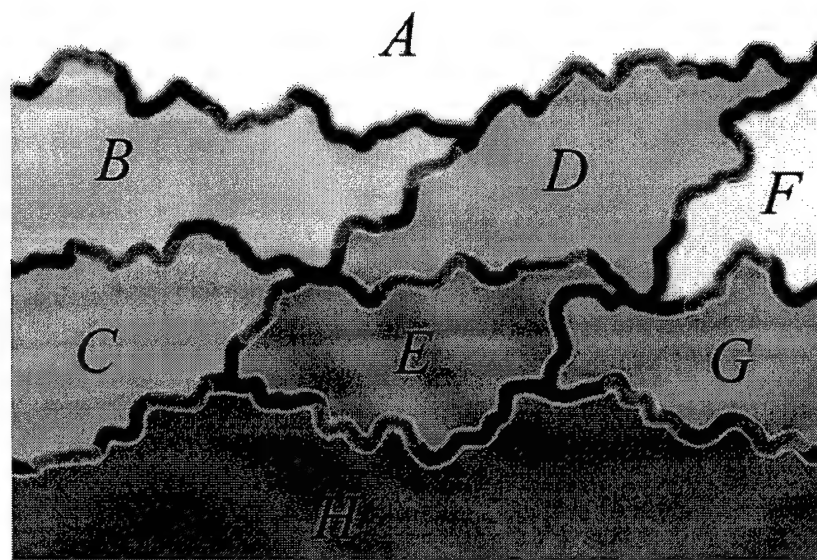
*AIAA Journal*, Catrakis & Aguirre, Figures 5a and b



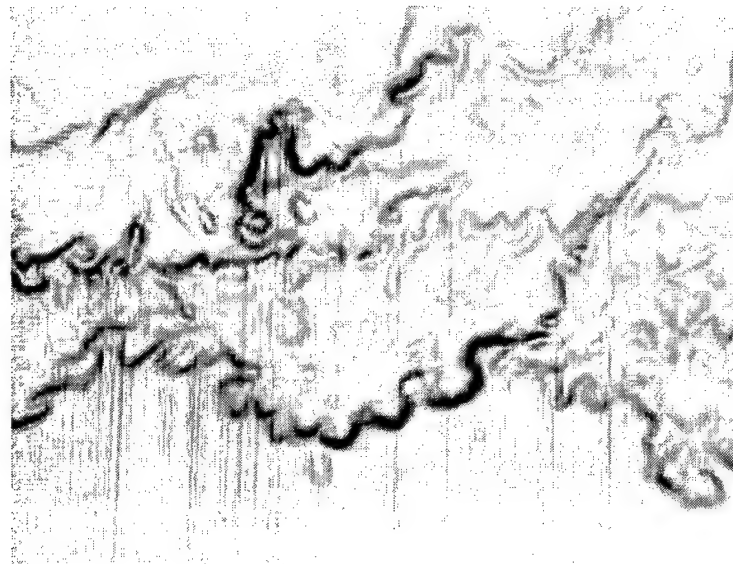
*AIAA Journal*, Catrakis & Aguirre, Figures 6a and b



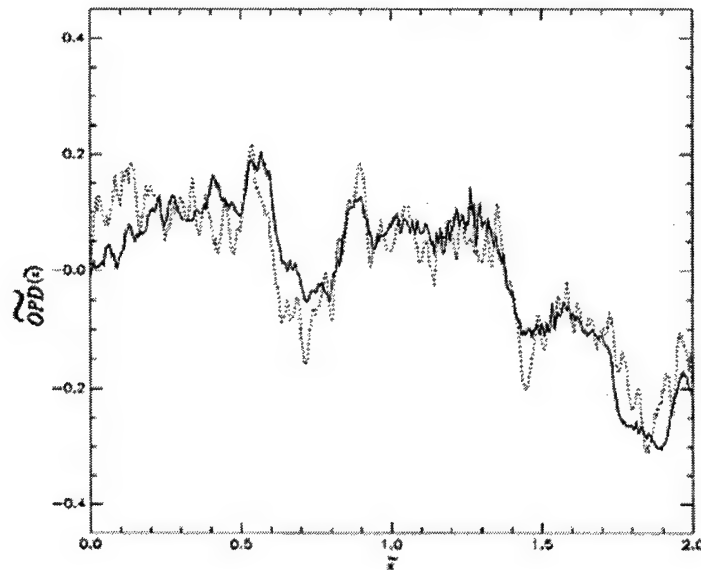
*AIAA Journal*, Catrakis & Aguirre, Figure 7



*AIAA Journal*, Catrakis & Aguirre, Figure 8



AIAA Journal, Catrakis & Aguirre, Figure 9



## Aerooptical Wavefronts and Scale-Local Characterization in Large-Reynolds-Number Compressible Turbulence

Haris J. Catrakis\*, Roberto C. Aguirre†, and Jennifer C. Nathman†

*Aeronautics and Fluid Dynamics Laboratories*

*University of California, Irvine, CA 92697*

### Abstract

A new technique is proposed which enables the scale-local characterization of aerooptical wavefronts. Because optical wavefronts degraded by turbulent flows are physically highly anisotropic and exhibit distortions over a wide range of scales, a method is needed to examine the wavefront structure at varying degrees of anisotropy and as a function of scale. We introduce an aerooptical-wavefront-anisotropy (AWA) parameter as the ratio of scaling factors for the wavefront distortions and for the wavefront transverse extent. This AWA parameter, combined with box counting, enables a scale-local anisotropic examination of the wavefronts. We demonstrate this technique on wavefronts derived from experiments on large-Reynolds-number ( $Re \sim 10^6$ ) high-compressibility ( $M_c \sim 1$ ) turbulent shear layers between optically-different gases. Variation of the AWA parameter and scale-local examination of the distortions reveal the presence of anisotropic self-similarity, or self-affinity, at small scales spanning nearly a decade. This finding shows the utility of the technique to detect scaling in large-Reynolds-number flow experiments from the aerooptical behavior. The present finding and technique provide the key ingredients to extrapolate the small-scale properties of compressible-flow aerooptical wavefronts to higher Reynolds numbers, and are also useful for modeling and for computational aerooptics.

### 1. Introduction

The large-scale properties of aerooptical interactions in turbulent flows can be expected to be strongly dependent on the flow geometry and boundary conditions (e.g. Truman & Lee<sup>1</sup>; Dimotakis, Catrakis, & Fourguette<sup>2</sup>; Jumper & Fitzgerald<sup>3</sup> and references therein). In

---

\*Assistant Professor, Member AIAA, Corresp. Author, E-mail: catrakis@uci.edu, Tel: (949) 378-7781.

†Graduate Student, Member AIAA.

contrast, at least at large Reynolds numbers and for incompressible flow conditions, there is evidence that the small-scale flow structure can exhibit scaling or self-similar behavior which is weakly, if at all, sensitive to the flow geometry, in the sense that small-scale turbulence statistics appear to be independent of the flow geometry or large-scale behavior to a good approximation (e.g. Sreenivasan<sup>4</sup>; Catrakis, Aguirre, & Ruiz-Plancarte<sup>5</sup>). The Reynolds number needs to be sufficiently large for the turbulent behavior to be fully-developed. This requires at a minimum that the Reynolds number  $Re$  based on the large scales must be at least  $Re \gtrsim 10^4$  (e.g. Dimotakis<sup>6</sup>). In airborne applications requiring high-resolution long-range optical imaging or beam propagation, which are necessarily associated with large Reynolds numbers, a complete description requires knowledge of both the small-scale properties and the large-scale behavior.

A useful point of view in developing techniques to characterize as a function of scale highly-irregular objects, such as optical wavefronts or fluid interfaces in turbulence, is to examine geometric properties and particularly the extent to which self-similar/fractal behavior (e.g. Sreenivasan<sup>4</sup>; Villermaux & Innocenti<sup>7</sup>) or scale-dependent behavior (e.g. Catrakis & Dimotakis<sup>8</sup>) is exhibited at the small scales. Since the structure of aerooptical wavefronts is essentially determined by the turbulent flow structure, one may expect that the aerooptical distortions will exhibit self-similar behavior at small scales if the refractive fluid interfaces are self-similar. This has been suggested theoretically for optical wavefronts distorted by incompressible turbulent flows (e.g. Hentschel & Procaccia<sup>9</sup>; Schwartz, Baum, & Ribak<sup>10,11</sup>). For compressible flows, there is some evidence that the small-scale structure of fluid interfaces can exhibit self-similarity (e.g. unpublished work of Sreenivasan & Johnson cited in Smits & Dussauge<sup>12</sup>; Poggie<sup>13</sup>). Such self-similarity can be expected to be at most weakly dependent on the large-scale flow properties. Thus, for compressible turbulence, one might expect self-similar scaling behavior for the small-scale properties of both the turbulent fluid interfaces and the turbulence-distorted optical wavefronts. Self-similar behavior of the optical wavefronts, if found at high compressibility, would permit extrapolating the small-scale optical behavior to the large Reynolds numbers of interest in practical applications in high-speed flight.

In the present work, we introduce an aerooptical-wavefront-anisotropy (AWA) parameter defined as a ratio of scaling factors for the optical path difference (OPD) and for the

wavefront spatial extent. This is described in §2 in the context of the physical anisotropy of aerooptical wavefronts. The AWA parameter enables the examination of the small-scale geometrical properties of the wavefronts using an anisotropic extension of the box counting method and this is developed in §3. We demonstrate the utility of this technique on wavefront data derived from large-Reynolds-number high-compressibility shear layers between optically-different gases. A description of the experimental technique, and a discussion of the important issue of mixing vs. density effects in aerooptics, can be found in the companion paper (Catrakis & Aguirre<sup>14</sup>) and references therein. In §4 the results of the scale-local examination of the wavefront data are presented. The AWA parameter is found to be useful to discern anisotropically self-similar, or self-affine, behavior of the OPD at small scales. This scaling behavior can be expected in other large-Reynolds-number highly-compressible flows since the small-scale behavior is at most weakly dependent on the large-scale behavior, as long as the Reynolds number is large enough for the turbulent flow to be fully-developed. Consequences of the present findings are discussed, in the conclusions, regarding large-Reynolds-number experimental studies, modeling, and computational aerooptics. Considerations of the large-scale aerooptical distortions, using a new interfacial-fluid-thickness approach, are the subject of the companion paper (Catrakis & Aguirre<sup>14</sup>).

## 2. Aerooptical-wavefront-anisotropy (AWA) parameter in large-Reynolds-number turbulent flows

One of the practical as well as fundamental objectives in aerooptics is to develop the means to extrapolate the behavior of the optical-wavefront structure to larger Reynolds numbers, including effects of compressibility. Knowledge of the small-scale structure of aerooptical wavefronts is needed toward this objective. Optical wavefronts propagating through turbulent flows can be expected to exhibit behavior that is similar to, or related closely to, the flow structure. To be able to extrapolate the behavior of a turbulence-generated refractive-index field  $n(\mathbf{x}, t)$  to large Reynolds numbers, it is important that the Reynolds number of the flow under study be at least above the minimum value associated with the transition to fully-developed turbulence (e.g. Dimotakis<sup>6</sup>), i.e.

$$Re \gtrsim 10^4. \quad (1)$$

As long as the turbulent flow is fully developed, i.e. satisfies at least the criterion in equa-

tion 1, the range of scales exhibited by the refractive field  $n(\mathbf{x}, t)$  increases with increasing Reynolds number, as is well known, as,

$$\frac{\lambda_{\max}}{\lambda_{\min}} \sim Re^{3/4}, \quad (2)$$

for gas-phase flows (Kolmogorov<sup>15</sup>), where  $\lambda_{\min}$  is the smallest scale or Kolmogorov scale and  $\lambda_{\max}$  is the largest scale identified as the extent of the flow region through which the wavefronts propagate or alternatively as the extent of large-scale shear in the flow. An important issue, in the context of the present work, is that there is a narrower range of scales, which appears only for large-Reynolds-number flows and refractive-index fields, and this is the range of scales bounded from above by the Liepmann-Taylor scale  $\lambda_{LT}$  and from below by  $\lambda_{\min}$ , i.e.,

$$\lambda_{\min} \lesssim \lambda \lesssim \lambda_{LT} \sim \lambda_{\max} Re^{-1/2}, \quad (3)$$

where similarity properties (e.g. Kolmogorov<sup>15</sup>), including possibly self-similarity (e.g. Sreenivasan<sup>4</sup>), are present. The Liepmann-Taylor scale  $\lambda_{LT}$  denotes the largest of the small scales that are not directly affected by large-scale effects or, equivalently, the smallest scale that is directly affected by large-scale effects. Such properties are important because they can be expected to help extrapolate aerooptical behavior to larger Reynolds numbers, encountered in practice, in both incompressible and compressible flows (e.g. Smits & Dussauge<sup>12</sup>).

In order to characterize aerooptical distortions over the wide range of scales associated with large values of the Reynolds number (cf. equations 1-3), techniques are needed that enable the description of optical-wavefront structure as a function of scale. Most previous studies of the small-scale flow behavior and of the optical-wavefront behavior have focused on spectral descriptions or, equivalently, on descriptions based on second-order structure functions (e.g. Andrews & Phillips<sup>16</sup>; Dimotakis, Catrakis, & Fourguette<sup>2</sup>). Spectral descriptions, however, characterize the aerooptical behavior in Fourier space and do not uniquely identify the geometrical structure of the turbulent flow or optical wavefronts. This is because power spectra retain no phase information. The description of the geometrical structure of turbulent flows in physical space is a relatively-recent development (e.g. Sreenivasan<sup>4</sup>; Catrakis, Aguirre, & Ruiz-Plancarte<sup>5</sup>) and relies on box-counting techniques. A generalized version of the box-counting technique, that can characterize anisotropic surfaces such as optical wavefronts, will be proposed and described in §3. In the present section, the issue

of optical-wavefront anisotropy will be first addressed as it is a crucial physical aspect of wavefront structure and an important ingredient of the new box-counting technique of §3.

The governing equation for the propagation of optical wavefronts, at the level of description of geometrical optics, is the eikonal equation for the optical path length (OPL) or, equivalently, the inverse or solution to the eikonal equation which is the integral for the OPL in terms of the refractive index along the optical beam propagation path, i.e.

$$|\nabla(\text{OPL})| = n, \quad \text{or}, \quad \text{OPL}(\mathbf{x}, t) \equiv \int_{\text{ray}} n(\ell, t) d\ell \equiv \int_{\text{ray}} n(\ell, t) h_{n,\ell} |dn|, \quad (4)$$

where the first integral is over the physical distance  $\ell$  along the propagation path. In the second integral, the OPL is expressed directly in terms of the effective refractive interfacial fluid thickness (IFT) which is  $h_{n,\ell} = 1/|\nabla n|_\ell$  (Catrakis & Aguirre<sup>14</sup>). As usual, the refractive index is  $n = c_0/c$ , where  $c_0$  is the speed of light in vacuum and  $c$  is the local speed of light. Since the velocity of light is related to the propagation distance through  $c = d\ell/dt$ , we can also express the OPL integral as  $\text{OPL} = \int n d\ell = c_0 \int (1/c) d\ell = c_0 \int dt$ , i.e. it follows that the OPL integral is essentially the integrated propagation time, or wavefront travel time, even though the integral is originally defined as a spatial integral.

In the present work, the emphasis is on the optical-wavefront structure. The optical wavefronts are physically the isosurfaces of the OPL, i.e.

$$\text{OPL}(\mathbf{x}, t) = \text{const..} \quad (5)$$

This simple and important statement is clear physically because, as stated above, the OPL integral is essentially a propagation-time integral, i.e.  $(\text{OPL})/c_0 = \int dt$ . A surface of constant OPL is, therefore, a surface on which all points have travelled over the same propagation time, ie. duration, and therefore this surface is the wavefront. By simply normalizing the OPL, one can see that the OPL integral is also essentially an optical-phase integral. We see, therefore, that isosurfaces of the OPL, or of the travel time, or of the optical phase, are all equivalent physical representations of the optical wavefronts. It is noteworthy to recall, in contrast, that the wavefront-location integral  $\int c dt = \int d\ell$  does not of course have this property, i.e. its isosurfaces do not represent the wavefronts, since the isosurfaces of the wavefront-location integral are just surfaces of constant propagation distance. This il-

lustrates what is perhaps the most important physical property of the OPL integral, i.e. that the OPL integral is physically and intuitively very helpful precisely because it has the property that the OPL isosurfaces are the wavefronts themselves.

In turbulent flows, and especially at large Reynolds numbers, the OPL isosurfaces or wavefronts can be expected to be highly irregular. In the present work, our objective is to characterize the physical structure of the optical wavefronts as a function of scale allowing for anisotropic scaling behavior. The first issue that needs to be addressed is that aerooptical wavefronts are physically highly-anisotropic surfaces. This is because, without any normalization, the spatial transverse extents of the optical wavefronts are in practice much larger than the OPL variations. This is especially so because the refractive-index variations, e.g. as quantified by the root-mean-square magnitude, are relatively small when compared to unity for gas-phase flows. Consequently, as the integrals in equation 4 suggest, the OPL variations will be much smaller than the spatial transverse extent (i.e. aperture) of any optical beam in practice. The OPL variations are best expressed through the optical path difference (OPD) where  $\text{OPD} = \text{OPL} - \int_{\text{ray}} n_{\text{ref}}(\mathbf{x}, t) d\ell$ , where  $n_{\text{ref}}$  denotes a reference refractive index, e.g. corresponding to a freestream condition. Physically, therefore, the wavefront anisotropy is present because,

$$|\Delta n|_{\text{rms}} \ll 1, \quad \text{and}, \quad \text{OPD}_{\text{rms}} \ll |\Delta\ell|, \quad (6)$$

where  $|\Delta n|_{\text{rms}}$  and  $\text{OPD}_{\text{rms}}$  denote respectively the root-mean-square magnitudes of the refractive-index variations and of the OPD of the distorted wavefront, and  $|\Delta\ell|$  denotes a measure of the total optical-beam-propagation path which is  $|\Delta\ell| \sim L$  or  $\lambda_{\max}$ , i.e. comparable to the large-scale extent  $L$  of the flow as far as the aerooptical interactions in the turbulent region are concerned. This strong anisotropy of aerooptical wavefronts refers to their physical, unnormalized structure. One may normalize the OPD so that the effective degree of anisotropy can change. By also scaling the spatial coordinates, one can examine the wavefronts at varying degrees of anisotropy, as will be shown below and in §3.

A schematic showing a planar wavefront incident on a three-dimensional optically-active turbulent-flow region and the irregular wavefront emerging from the flow in three dimensions is depicted in figure 1. The distorted wavefront is highly irregular and highly anisotropic. We can also consider the OPL or OPD profiles, which are themselves highly irregular. The ideas below are applicable to both the wavefront surfaces and the OPL or OPD profiles. Taking

the  $x$ - and  $y$ -directions as the spatial directions perpendicular to the incident-wavefront propagation direction, the OPD profiles are in this case functions of  $x$  and  $y$  as well as time, i.e.

$$\text{OPD}(x, y, t), \quad (7)$$

where, for simplicity of notation in what follows below,  $x$  and  $y$  are the spatial coordinates normalized by the large-scale transverse extent  $L$  of the flow (cf. figure 1), and OPD will denote the optical path difference normalized by  $(\Delta n)_{\text{ref}} L$  with  $(\Delta n)_{\text{ref}}$  denoting the reference (freestream-based) refractive-index difference. To be able to vary the anisotropy of the OPD, which will be needed in §§ 3 and 4, we propose the use of scaling factors (stretching factors) for both the OPD and the spatial-extent coordinates, i.e. so that the anisotropic transformation of the optical-wavefront surface can be represented as

$$\text{OPD}(x, y, t) \longrightarrow \alpha_{\text{OPD}} \text{OPD}(\alpha_x x, \alpha_y y, t), \quad (8)$$

where  $\alpha_{\text{OPD}}$  is a scaling factor for the OPD, and  $\{\alpha_x, \alpha_y\}$  are scaling factors for the spatial-extent coordinates normal to the incident-wavefront propagation direction. These scaling factors can each be greater than or less than unity. Two examples are shown in figure 2 where different values of  $\alpha_{\text{OPD}}$  are employed for the same wavefront or OPD isosurface. We note, with regard to equation 8, that only two wavefront-anisotropy parameters are needed (only the ratios matter) and, therefore, we define a (vector) aerooptical-wavefront-anisotropy (AWA) parameter given by

$$\boldsymbol{\alpha} \equiv \left\{ \frac{\alpha_{\text{OPD}}}{\alpha_x}, \frac{\alpha_{\text{OPD}}}{\alpha_y} \right\}, \quad (9)$$

in terms of the ratios of the scaling factor of the OPD to each of the scaling factors of the transverse spatial coordinates. For a wavefront in 2-D space, e.g. in figures 3a and b, only one scaling factor is needed, e.g. the AWA parameter becomes  $\alpha \equiv \alpha_{\text{OPD}}/\alpha_x$ . The proposed AWA parameter  $\boldsymbol{\alpha}$  enables the variation of the effective anisotropy of aerooptical wavefronts, which can be used to examine their structure as a function of scale as will be shown in §§ 3 and 4. We note that the AWA parameter can be used not only in the study of the OPD isosurfaces but also in the study of the OPD field itself, if needed.

As mentioned above, the present anisotropy considerations are applicable to both the wavefront itself and to the OPL or OPD profiles. The proposed AWA parameter, therefore,

is also applicable to both. In practice, it is important to appreciate that while the OPL isosurfaces represent the wavefronts, what is more straightforward to measure experimentally is the OPL or OPD profile, i.e. the variation of the OPL in the reference measurement plane of a detector or along a reference line. It is helpful, however, to also appreciate that the OPL isosurfaces are, after all, derivable from the OPL field assuming the OPL field is known. For example, considering wavefronts that emerge from a turbulent shear flow and subsequently propagate in a near-field region of uniform reference refractive index, the wavefronts will propagate at a constant speed in the uniform-index region. As long as this region is in the near field, i.e. without having to consider far-field propagation effects, the normalized OPL profiles are geometrically equivalent to the OPL isosurfaces. The wavefront-anisotropy considerations above, and the AWA parameter, are equally applicable to the profiles as well as isosurfaces of the OPL or OPD fields.

### 3. Anisotropic box-counting technique for characterization of aerooptical wavefronts

To investigate the physical structure of optical wavefronts, a useful approach is to conduct box counting which enables an examination of the manner in which the wavefronts' geometrical features vary with scale (e.g. Catrakis *et al.*<sup>17</sup>; Catrakis & Aguirre<sup>18</sup>). For each wavefront, a bounding box or rectangle is identified and partitioned successively into smaller boxes. The number of boxes containing the wavefront is counted at each box scale  $\lambda$ . This coverage count, denoted as  $N_d(\lambda)$  in  $d$  dimensions, can be used to quantify the geometric structure as a function of scale. At the largest scale  $\lambda_{\max}$ , the coverage count is unity, i.e.  $N_d(\lambda_{\max}) = 1$ . We sometimes also denote the largest scale as  $\delta$ , i.e. the bounding-box scale. One can normalize the coverage count by the total number of boxes available at each scale  $\lambda$  and this is known as the coverage fraction,

$$F_d(\lambda) = \left( \frac{\lambda}{\lambda_{\max}} \right)^d N_d(\lambda), \quad (10)$$

where  $0 \leq F_d(\lambda) \leq 1$  and the limiting values correspond to the smallest and largest scales, respectively. The physical meaning of the coverage fraction is that it is the geometric probability of finding a part of the wavefront in a  $\lambda$ -scale box. A larger value of  $F_d(\lambda)$ , at a given scale, indicates a more irregular wavefront structure at that scale.

Highly-anisotropic behavior can be expected for aerooptical wavefronts (cf. §2) and, because of this, the scale  $\lambda$  must be treated as a vector in general, as was proposed for turbulent fluid interfaces in general by Catrakis<sup>19</sup>. In the present case,

$$\boldsymbol{\lambda} = \{\lambda_{\text{OPD}}, \lambda_x, \lambda_y\}, \quad (11)$$

with the (scalar) box size  $\lambda$  denoting in the general case the magnitude of  $\boldsymbol{\lambda}$ . In 3-D space, for example, we can write this as

$$\lambda = (\lambda_{\text{OPD}} \lambda_x \lambda_y)^{1/3}, \quad (12)$$

where  $\lambda_{\text{OPD}}$  denotes the extent of each box along the OPD axis and  $\{\lambda_x, \lambda_y\}$  denote the spatial extents of each box in the  $\{x, y\}$  directions. The advantage of a scale magnitude defined as in equation 12 is that  $\lambda^3$  can be identified as a volume occupied by each  $\lambda$ -sized box.

The most important quantity that the box-counting technique produces is the coverage dimension  $D_d(\lambda)$  as a function of the scale magnitude  $\lambda$ . The coverage dimension can be computed as the fractional increase in the coverage count per unit fractional decrease in scale, or equivalently the logarithmic derivative of the coverage count with scale, i.e.

$$D_d(\lambda) \equiv -\frac{dN_d(\lambda)/N_d(\lambda)}{d\lambda/\lambda} = -\frac{d \log N_d(\lambda)}{d \log \lambda}. \quad (13)$$

and can be interpreted as a fractional (fractal) dimension whose departure from the topological dimension  $d_t$  of the wavefronts quantifies how complex the wavefront structure is. The coverage dimension must be in the range

$$d_t \leq D_d(\lambda) \leq d, \quad (14)$$

for optical wavefronts. In particular, at the smallest scales and largest scales respectively the coverage dimension reaches those limits, i.e.

$$D_d(\lambda) \rightarrow d_t \quad \text{as} \quad \lambda \rightarrow \lambda_{\min}, \quad \text{and,} \quad D_d(\lambda) \rightarrow d \quad \text{as} \quad \lambda \rightarrow \lambda_{\max}. \quad (15)$$

For optical wavefronts in 3-D, as indicated in figure 1, these limiting values become  $d_t = 2$

and  $d = 3$  respectively. For wavefronts in 2-D, cf. figure 3, these values become  $d_t = 1$  and  $d = 2$  respectively. It is also helpful to think of the *relative coverage dimension* of the wavefronts, i.e. the coverage dimension relative to the topological dimension, which is given by  $D_d(\lambda) - d_t$  in general, or  $D_2(\lambda) - 1$  in 2-D for example. This is useful for comparing wavefront structure in different dimensions, e.g. in 3-D vs. 2-D, because the values of the relative coverage dimension must range from 0 to 1 independent of whether the wavefront is in a 3-D or 2-D region of the flow, cf. equation 15. Recalling that at large Reynolds numbers one may expect similarity properties over a wide range of scales (cf. equation 3), another important use of the coverage dimension is that it can reveal such similarity properties, including the presence of self-similarity.

If the coverage dimension  $D_d(\lambda)$  is a constant over a wide range of scales, then this would mean that the wavefront physically has scale-independent structure in that range of scales and then the wavefront could be modeled using this self-similarity. Specifically, for self-similar behavior the coverage dimension would be  $D_d(\lambda) = D_d = \text{const.}$  and the structure of the wavefront could be extrapolated to larger Reynolds numbers (cf. equation 2) using

$$N_d(\lambda) \sim \left( \frac{\lambda_{\max}}{\lambda} \right)^{D_d}, \quad (16)$$

over a range of scales  $\lambda_{\min} \lesssim \lambda \lesssim \lambda_{\text{LT}}$ , cf. equation 3. The value of  $D_d$  would reflect the complexity of the wavefront structure that statistically repeats itself over a range of scales.

If, however, the coverage dimension is found to be a continuous function of scale throughout the range of scales, then the coverage count would no longer be a power law but instead would behave as

$$N_d(\lambda) = \exp \left\{ \int_{\lambda}^{\lambda_{\max}} D_d(\lambda') \frac{d\lambda'}{\lambda'} \right\}, \quad (17)$$

as can be readily seen by inverting equation 10. Such scale-dependent behavior, where for example the coverage dimension could be increasing with increasing scale over a range of scales, would mean that the complexity of the wavefront varies with scale. This would mean that more complicated, scale-dependent models would be needed to extrapolate the small-scale structure of optical wavefronts to larger Reynolds numbers. We note, however, that scale-dependent behavior on the basis of  $D_d(\lambda)$  alone may not necessarily imply lack of self-similarity. Recent work has indicated that other scale-local measures may be needed

to discern self-similar behavior in those cases where  $D_d(\lambda)$  appears to be scale dependent (Catrakis, Aguirre, & Ruiz-Plancarte<sup>5</sup>). In the cases, however, where there is clear evidence of scale independence in  $D_d(\lambda)$ , this quantity is sufficient to detect self-similarity.

As emphasized in §2, aerooptical wavefronts can be expected to exhibit a strong anisotropy. A more general box-counting approach therefore is needed, to be useful for aerooptics, where one can examine the box-counting behavior of the wavefronts allowing for the possibility that they may be scale independent, i.e. self-similar, in an anisotropic manner. Self-similar anisotropic behavior is sometimes also called self-affine behavior. Irregular self-affine objects exhibit structure which is scale independent but in a manner that depends on the direction. In other words, self-affine objects are anisotropically scale independent whereas self-similar objects are isotropically scale independent.

We propose an anisotropic extension of the box-counting technique whereby the AWA parameter  $\alpha$  of §2 becomes a parameter in the coverage count and consequently in the coverage fraction as well as in the coverage dimension, i.e.

$$N_d(\lambda; \alpha), \quad \text{and}, \quad F_d(\lambda; \alpha), \quad \text{with}, \quad D_d(\lambda; \alpha) = -\frac{d \log N_d(\lambda; \alpha)}{d \log \lambda}. \quad (18)$$

The introduction of the AWA parameter  $\alpha$  in the coverage quantities makes possible a practical examination of anisotropic structure. We note that an equivalent way to proceed would be to treat the scale  $\lambda$  as a vector  $\lambda$  (cf. equation 11) and then to define the coverage dimension through an extension of equation 13. This, however, would lead to coverage-dimension vectors expressed as partial derivatives of the coverage count. The proposed approach, i.e. using the quantities in equation 18, offers instead a much simpler way to characterize the anisotropic structure of aerooptical wavefronts, with a coverage dimension that is scalar valued rather than vector valued.

As an example in 2-D, figures 4a and b show the same optical wavefront at two different values of the AWA parameter  $\alpha$  with the boxes necessary to cover the wavefront in each case for several different scales. The corresponding coverage results are shown in figures 5a, b, and c. Note that the choice of the values of the AWA parameter, in figures 4a and b, is such that they both have the same scale magnitudes, i.e. the value of  $(\alpha_{OPL} \alpha_x)^{1/2}$  is the same for both examples. This was done so that any effects of the largest scales are removed in order to

focus on the small-scale structures. Significantly, we see that for the *same* optical wavefront examined under *different* levels of anisotropy, *different behavior* is evident at the *small scales* in figure 5c. This is an important observation because it illustrates that this technique is sensitive to the presence of anisotropy at small scales and, therefore, one can expect to be able to use it to examine aerooptical wavefronts at large Reynolds numbers as will be done in §4. It is also important to appreciate that the above ideas can be expected to be useful to examine not only the ensemble-averaged behavior of the instantaneous wavefronts but also the *instantaneous* wavefront structure itself. The latter is, of course, crucial in practical aerooptics applications.

#### 4. Scale-local structure of aerooptical distortions at large Reynolds number and high compressibility

In this section, we demonstrate the use of the proposed anisotropic box-counting technique for the characterization of the scale-local structure of aerooptical distortions. We are particularly interested in the behavior at large Reynolds numbers and high compressibility because this is a flow regime of practical interest in a number of aerooptics applications in high-speed flight, and also because previous work suggests that high-compressibility turbulent flows exhibit important differences at least at the large scales when compared to incompressible or weakly-compressible turbulent flows (e.g. Samimy & Elliot<sup>20</sup>; Pampouschou<sup>21</sup>). Less is known about the effect of compressibility on the small-scale behavior at large Reynolds numbers. Computational results are available on compressible turbulent flows (e.g. Porter, Woodward, & Pouquet<sup>22</sup>) but are presently restricted to low Reynolds numbers. On the theoretical side, there are proposals of similarity and self-similarity properties at large Reynolds numbers (e.g. Sreenivasan<sup>4</sup>) that have been put forth for incompressible turbulence. However, it is presently not clear to what extent such incompressible-turbulence similarity properties are applicable at compressible-flow conditions including high compressibility.

To examine the applicability of the technique proposed in §§ 2-3, we employ recent wavefront data derived from experimental studies of aerooptical distortions in high-compressibility shear layers between different gases (Dimotakis, Catrakis, & Fourguette<sup>2</sup>). A discussion of the experimental technique can be found in the companion paper (Catrakis & Aguirre<sup>14</sup>) with a more complete description in Dimotakis, Catrakis, & Fourguette<sup>2</sup>). The aerooptical

behavior in these measurements is dominated by mixing effects. The important issue of mixing vs. density effects in aero optics is discussed in Jumper & Fitzgerald<sup>3</sup> and also in the companion paper to the present work (Catrakis & Aguirre<sup>14</sup>). For the data employed here, a large-scale Reynolds number of  $Re \sim 10^6$  and a convective Mach number of  $M_c \sim 1$  were achieved and the OPD profiles corresponding to wavefronts emerging normal to the shear layers were derived by Fourier filtering the refractive-index field, as described in Dimotakis, Catrakis, & Fourguette<sup>2</sup>. Examples of the OPD profiles at the high-compressibility flow conditions are shown in figures 6a, b, and c. The optical-wavefront distortions correspond to the aero optical interactions in a two-dimensional plane transverse to the shear layer. The incident wavefronts are initially linear, i.e. straight, and subsequently propagate transverse to the flow, from one freestream to the other, through two-dimensional spatial streamwise slices of the flow. The wavefront OPD profiles correspond to the aero optical wavefronts that emerge from the turbulent flow region. Although the wavefront data in figures 6a and b are not fully resolved, the resolution is sufficient to capture a large fraction of the full range of scales at these large Reynolds numbers. This fraction of the range of scales is estimated to be  $\sim 500 : 1$  based on the camera pixel resolution which was employed to record the flow images from which the OPD profiles were derived. Keeping in mind that similarity properties are not expected throughout the entire range of scales smaller than the large scale, but rather in a fraction of those scales (cf. equation 3), these data can be expected to be useful to examine the presence of similarity or self-similarity in the wavefront structure.

For the shear-layer data, the OPD profiles are functions of the streamwise coordinate  $x$  normalized by the transverse extent  $L$  of the large-scale shear in this flow, i.e.

$$\text{OPD} \left( \frac{x}{L} \right) . \quad (19)$$

The incident wavefronts are assumed to be planar (linear in the planar slice of the flow studied) so that the coverage dimension is

$$D_2(\lambda) = 1 , \quad (20)$$

prior to propagation of the wavefronts through the shear layer. Subsequent to propagation and distortion of the wavefronts, the relevant AWA parameter associated with the OPD

profile is

$$\alpha \equiv \frac{\alpha_{\text{OPD}}}{\alpha_x}, \quad (21)$$

(cf. §2 and equations 8-9), corresponding to the two-parameter stretched-OPD profile, i.e.

$$\alpha_{\text{OPD}} \text{ OPD} \left( \alpha_x \frac{x}{L} \right). \quad (22)$$

As pointed out in §2, the two parameters  $\alpha_{\text{OPD}}$  and  $\alpha_x$  are equivalent to the single AWA parameter  $\alpha = \alpha_{\text{OPD}}/\alpha_x$ . One parameter is sufficient, for wavefronts in 2-D space, to permit an examination of the wavefront structure at different levels of anisotropy.

Box counting was performed on the high-compressibility shear-layer wavefront profiles for several different values of the AWA parameter  $\alpha$ , over the range  $0.3 \lesssim \alpha \lesssim 3$ , i.e. spanning one order of magnitude in the AWA parameter. For each value of  $\alpha$ , the wavefront was stretched and subsequently partitioned into boxes (tiles in 2-D) so that the box count was computed as a function of scale, i.e.

$$N_2(\lambda; \alpha), \quad (23)$$

where the subscript 2 denotes that these data are spatially two-dimensional. From the coverage count, we computed the coverage fraction and the coverage dimension as a function of scale, i.e.

$$F_2(\lambda; \alpha) = \left( \frac{\lambda}{\lambda_{\max}} \right)^2 N_2(\lambda; \alpha), \quad \text{and}, \quad D_2(\lambda; \alpha) = - \frac{d \log N_2(\lambda; \alpha)}{d \log \lambda}. \quad (24)$$

Two important observations were made:

- (a) *the small-scale wavefront behavior depends strongly on the AWA parameter  $\alpha$ , and*
- (b) *there exists a particular value of the AWA parameter  $\alpha = \alpha^*$  for which the small-scale wavefront structure is found to be scale independent over a range of scales.*

The first observation confirms the idea in § 2 that aerooptical wavefronts are highly anisotropic and shows that the technique described in § 3 is capable of detecting the dependence of the small-scale structure on this anisotropy. The second observation, i.e. that there is scale independence over a range of scales for a particular value  $\alpha^*$ , which is found to be  $\alpha^* \simeq 0.9$  for the present data, is particularly important. The results are shown in figures 7a, b, and

c, that depict respectively the coverage count  $N_2(\lambda; \alpha^*)$ , coverage fraction  $F_2(\lambda; \alpha^*)$ , and the relative coverage dimension  $D_2(\lambda; \alpha^*) - 1$  for the critical value of the AWA parameter. For values of  $\alpha$  smaller than or greater than  $\alpha^*$ , qualitatively-different behavior was observed. Specifically,

- (a) for  $\alpha < \alpha^*$ , the wavefront structure is scale dependent with relatively-smaller values of the coverage dimension at intermediate scales,
- (b) there exists a particular value of the AWA parameter  $\alpha = \alpha^*$  for which the small-scale wavefront structure is found to be scale independent over a range of intermediate scales.
- (c) for  $\alpha > \alpha^*$ , the wavefront structure is scale dependent with relatively-larger values of the coverage dimension at intermediate scales.

The significance of the observed behavior at  $\alpha = \alpha^*$  is that this shows the presence of an intermediate range of small scales in which the wavefront is self-similar, i.e. a range of scales in which the coverage dimension is nearly a constant:

$$D_2(\lambda; \alpha^*) \simeq \text{const.} \simeq 1.27. \quad (25)$$

The uncertainty in the coverage dimension is estimated to be  $\pm 0.025$ , estimated from the variations between individual realizations. The  $D_2 \simeq 1.27$  value is found for the present flow conditions of high compressibility and large Reynolds number. At other flow conditions, e.g. different compressibility or Reynolds numbers, it may exhibit a dependence but this would be expected to be a weak dependence as long as the flow is fully developed. It can be noted that the  $D_2 \simeq 1.27$  value is lower than the  $D_2 \simeq 1.35$  value reported for incompressible flows (e.g. Sreenivasan<sup>4</sup>), and this is consistent with expectations that the dimension should decrease with increasing compressibility (e.g. Smits & Dussauge<sup>12</sup>). The present finding can be used to extrapolate the behavior to even larger Reynolds numbers at high compressibility, at least in shear layers, using

$$N_2(\lambda; \alpha^*) \sim \left( \frac{\lambda_{\max}}{\lambda} \right)^{1.27}, \quad (26)$$

(cf. equation 16). From figure 7c, we see that the self-similar behavior is evident in the measurements over a range of scales that span approximately one decade. Even though the

Reynolds number associated with the shear layer is large, i.e.  $Re \sim 10^6$ , and corresponds to a full range of flow scales given by  $\lambda_{\max}/\lambda_{\min} = Re^{3/4} \sim 3 \times 10^4$ , the range of scales over which similarity is expected is smaller. For example, a conservative estimate (Dimotakis<sup>6</sup>) is the ratio of the Liepmann-Taylor scale  $\lambda_{LT}$  to the Kolmogorov scale  $\lambda_K$  which grows slowly with Reynolds number, specifically  $\lambda_{LT}/\lambda_K \sim Re^{1/4} \sim 10$ , cf. equations 2 and 3 in §2. This estimate, at least of the extent of the range of self-similar scales, is closer to the presently-observed behavior (cf. figure 7c). Higher-resolution measurements would be needed to discern this issue further, i.e. whether the range of scales exhibiting self-similar behavior extends to smaller scales yet. We note that the critical value  $\alpha^*$  of the AWA parameter might depend to some extent on the Reynolds number and/or Mach number, and possibly on the flow boundary conditions. However, as long as the Reynolds number is large, i.e. meets the criterion for fully-developed turbulence (cf. §2), one can expect that the small-scale structure of the wavefronts and the critical value of the AWA parameter will be at most weakly dependent on these flow parameters. This is because the small-scale structure at large Reynolds numbers is at most weakly sensitive to the large-scale behavior (e.g. Sreenivasan<sup>4</sup>, Dimotakis<sup>6</sup>, and references therein).

The present finding of scale independence of the small-scale optical-wavefront structure over a range of scales at high compressibility provides experimental evidence that self-similarity is present in aerooptical interactions at high-compressibility flow conditions. Computational studies of compressible flows at low Reynolds numbers have indicated inertial-range scaling based on power spectra (e.g. Porter, Woodward, & Pouquet<sup>22</sup>) and this supports the present finding of self-similarity, although spectral behavior alone cannot be related uniquely to the physical structure of the fluid interfaces. The present observation of self-similar behavior in the physical structure of the distorted aerooptical wavefronts indicates that turbulent fluid interfaces at high compressibility also possess self-similarity properties. Self-similar behavior of the fluid interfaces would be sufficient to explain the observed self-similar aerooptical behavior, with anisotropy inherent in the wavefront OPD, cf. §2. Quantification and modeling of the physical structure of optical wavefronts, in real space as opposed to Fourier space, requires tools such as the technique presently demonstrated. The present results demonstrate that optical-wavefront self-similarity can be detected with the proposed approach using the AWA parameter.

## 5. Conclusions and implications

The proposed method of anisotropic box counting provides a technique useful for the scale-local characterization of the physical structure of aerooptical wavefronts, i.e. as a function of scale. The aerooptical-wavefront-anisotropy (AWA) parameter, defined as a ratio of scaling factors for the wavefront distortions and for the transverse extent of the wavefronts, combined with an anisotropic generalization of box counting enables a scale-local examination of wavefronts at varying degrees of anisotropy. This is particularly useful for the study of aerooptical wavefronts at large Reynolds numbers. Demonstration of this technique to experimental data in large-Reynolds-number ( $Re \sim 10^6$ ) high-compressibility ( $M_c \sim 1$ ) turbulent shear layers shows the presence of anisotropic self-similarity, or self-affinity, in the wavefront structure over a range of small scales spanning nearly a decade, as detected by varying the AWA parameter and conducting a scale-local examination of the distortions. Even though the data employed in this study are dominated by mixing effects as opposed to solely density effects, the anisotropy considerations and the AWA parameter can be expected to be useful in both cases.

The present finding and technique have helpful consequences for large-Reynolds-number experimental studies as well as modeling and computational studies. The data show the utility of the technique to detect scaling in large-Reynolds-number flow experiments using the optical behavior, and as such suggest an optical means to probe aspects of the mixing behavior at large Reynolds numbers. The present finding also provides a means to extrapolate the small-scale structure of optical distortions at high compressibility to larger Reynolds numbers. This can be expected to be useful in efforts to develop computational models and simulations of optical behavior in flows at large Reynolds numbers and high compressibility (e.g. Jones & Bender<sup>23</sup>). The present self-similarity model of the wavefront distortions suggests a key ingredient to help construct effective sub-grid-scale models in large-eddy simulations of aerooptical interactions. Small-scale properties of high-compressibility flows are also valuable because they can be coupled with descriptions that address the large-scale behavior of high-compressibility flows (e.g. the companion paper by Catrakis & Aguirre<sup>14</sup>), in order to develop frameworks that are capable of describing the behavior across the entire range of scales. Furthermore, this can provide the means to compare the cumulative effects of distortions at small scales to the effects at the large scales. These implications are

especially important in applications that require high-resolution optical imaging and beam propagation in high-speed flight.

## Acknowledgements

This work is supported by the Air Force Office of Scientific Research through Grants F49620-02-1-0142 and F49620-02-1-0277 (Dr. T. Beutner, Program Manager) and is part of a program on aerooptical interactions in turbulent flows. The authors are grateful to Prof. Eric Jumper, Prof. Ronald Hugo, Dr. Edward Fitzgerald, Dr. Michael Jones, and Prof. Randall Truman for helpful advice, and to Mr. Jesus Ruiz Plancarte for assistance with an earlier draft of this paper, as well as to the Reviewers for their insightful comments. Earlier versions of the anisotropy idea and box-counting technique described in this manuscript were presented by the authors as AIAA Paper 2001-2801 in Anaheim, California, and AIAA Paper 2002-2269 in Maui, Hawaii.

## References

- <sup>1</sup>Truman, C. R. and Lee, M. J., "Effects of organized turbulence structures on the phase distortion in a coherent optical beam propagating through a turbulent shear flow," *Phys. Fluids A*, Vol. 2, 1990, pp. 851–857.
- <sup>2</sup>Dimotakis, P. E., Catrakis, H. J., and Fourguette, D. C. L., "Flow structure and optical beam propagation in high-Reynolds-number gas-phase shear layers and jets," *J. Fluid Mech.*, Vol. 433, 2001, pp. 105–134.
- <sup>3</sup>Jumper, E. J. and Fitzgerald, E. J., "Recent advances in aero-optics," *Prog. Aerospace Sci.*, Vol. 37, 2001, pp. 299–339.
- <sup>4</sup>Sreenivasan, K. R., "Fractals and multifractals in fluid turbulence," *Annu. Rev. Fluid. Mech.*, Vol. 23, 1991, pp. 539–600.
- <sup>5</sup>Catrakis, H. J., Aguirre, R. C., and Ruiz-Plancarte, J., "Area-volume properties of fluid interfaces in turbulence: scale-local self-similarity and cumulative scale dependence," *J. Fluid Mech.*, Vol. 462, 2002, pp. 245–254.
- <sup>6</sup>Dimotakis, P. E., "Mixing transition in turbulent flows," *J. Fluid Mech.*, Vol. 409, 2000, pp. 69–98.
- <sup>7</sup>Villermaux, E. and Innocenti, C., "On the Geometry of Turbulent Mixing," *J. Fluid Mech.*, Vol. 393, 1999, pp. 123–147.

<sup>8</sup>Catrakis, H. J. and Dimotakis, P. E., "Mixing in turbulent jets: scalar measures and isosurface geometry," *J. Fluid Mech.*, Vol. 317, 1996, pp. 369–406.

<sup>9</sup>Hentschel, H. G. E. and Procaccia, I., "Passive scalar fluctuations in intermittent turbulence with applications to wave propagation," *Phys. Rev. A.*, Vol. 28, 1983, pp. 417–426.

<sup>10</sup>Schwartz, C., Baum, G., and Ribak, E. N., "Fractal character of turbulence-degraded wavefronts," *8<sup>th</sup> Meeting on Optical Engineering and Remote Sensing, SPIE Proceedings*, Vol. 1971, Tel Aviv, Israel, 1993, pp. 476–485.

<sup>11</sup>Schwartz, C., Baum, G., and Ribak, E. N., "Turbulence-degraded wave fronts as fractal surfaces," *J. Opt. Soc. Am.*, Vol. 11, No. 1, 1994, pp. 444–451.

<sup>12</sup>Smits, A. J. and Dussauge, J.-P., *Turbulent Shear Layers in Supersonic Flow*, AIP Press, 1996.

<sup>13</sup>Poggie, J., *Quantitative Flow Visualization Applied to the Study of Compressible Turbulent Flow*, Master's thesis, Princeton University, 1991.

<sup>14</sup>Catrakis, H. J. and Aguirre, R. C., "New interfacial-fluid-thickness approach in aerodynamics with applications to compressible turbulence," *AIAA J.*, 2004, forthcoming.

<sup>15</sup>Kolmogorov, A. N., "The local structure of turbulence in incompressible viscous fluid for very large Reynolds numbers," *Dokl. Akad. Nauka SSSR*, Vol. 30, 1941, pp. 301–305.

<sup>16</sup>Andrews, L. C. and Phillips, R. L., *Laser beam propagation through random media*, SPIE Optical Engineering Press, Bellingham, WA, 1998.

<sup>17</sup>Catrakis, H. J., Aguirre, R. C., Thayne, R. D., McDonald, B. A., and Hearn, J. W., "Are turbulence-degraded optical wavefronts and beam trajectories fractal?" *AIAA 32<sup>nd</sup> Plasmadynamics and Lasers Conference, AIAA 2001-2801*, Anaheim, CA, 2001.

<sup>18</sup>Catrakis, H. J. and Aguirre, R. C., "Inner-scale structure of turbulence-degraded optical wavefronts," *AIAA 33<sup>rd</sup> Plasmadynamics and Lasers Conference, AIAA 2002-2269*, Maui, HI, 2002.

<sup>19</sup>Catrakis, H. J., "Distribution of scales in turbulence," *Phys. Rev. E*, Vol. 62, 2000, pp. 564–578.

<sup>20</sup>Samimy, M. and Elliot, G. S., "Effects of compressibility on the characteristics of free shear layers," *AIAA J.*, Vol. 28, 1990, pp. 439–445.

<sup>21</sup>Papamoschou, D., "Structure of the compressible turbulent shear layer," *AIAA J.*, Vol. 29, 1991, pp. 680–681.

<sup>22</sup>Porter, D. H., Woodward, P. R., and Pouquet, A., "Inertial range structures in decaying compressible turbulent flows," *Phys. Fluids*, Vol. 10, 1998, pp. 237–245.

<sup>23</sup>Jones, M. and Bender, E. E., "CFD-based computer simulation of optical turbulence

through aircraft flowfields and wakes," *AIAA 32<sup>nd</sup> Plasmadynamics and Lasers Conference*, AIAA 2001-2798, Anaheim, CA, 2002.

Figure 1. Schematic of a planar optical wavefront (top) incident to a three-dimensional refractive-index field in a large-Reynolds-number turbulent compressible flow (middle), and the emerging highly-irregular aerooptical wavefront (bottom).

Figures 2a and b. Illustration of varying the effective anisotropy of an optical wavefront in 3-D using the proposed aerooptical-wavefront-anisotropy (AWA) parameter  $\alpha$ , cf. equations 8 and 9. The same wavefront is shown with  $|\alpha| \gg 1$  (top) and with  $|\alpha| \ll 1$  (bottom).

Figures 3a and b. Example of an optical wavefront in 2-D. The same wavefront is shown at two different values of the AWA parameter, which is a scalar-valued parameter in 2-D and is  $\alpha = \alpha_{\text{OPD}}/\alpha_x$ . In this example, the large-scale size of the wavefront bounding box is the same for each case, i.e.  $(\alpha_{\text{OPD}} \alpha_x)^{1/2}$  is the same.

Figure 4a. Illustration of the anisotropic box-counting technique for the wavefront as shown in figure 3a. Coverage boxes are shown at different scales. The coverage boxes are the boxes needed to completely contain the wavefront at each scale.

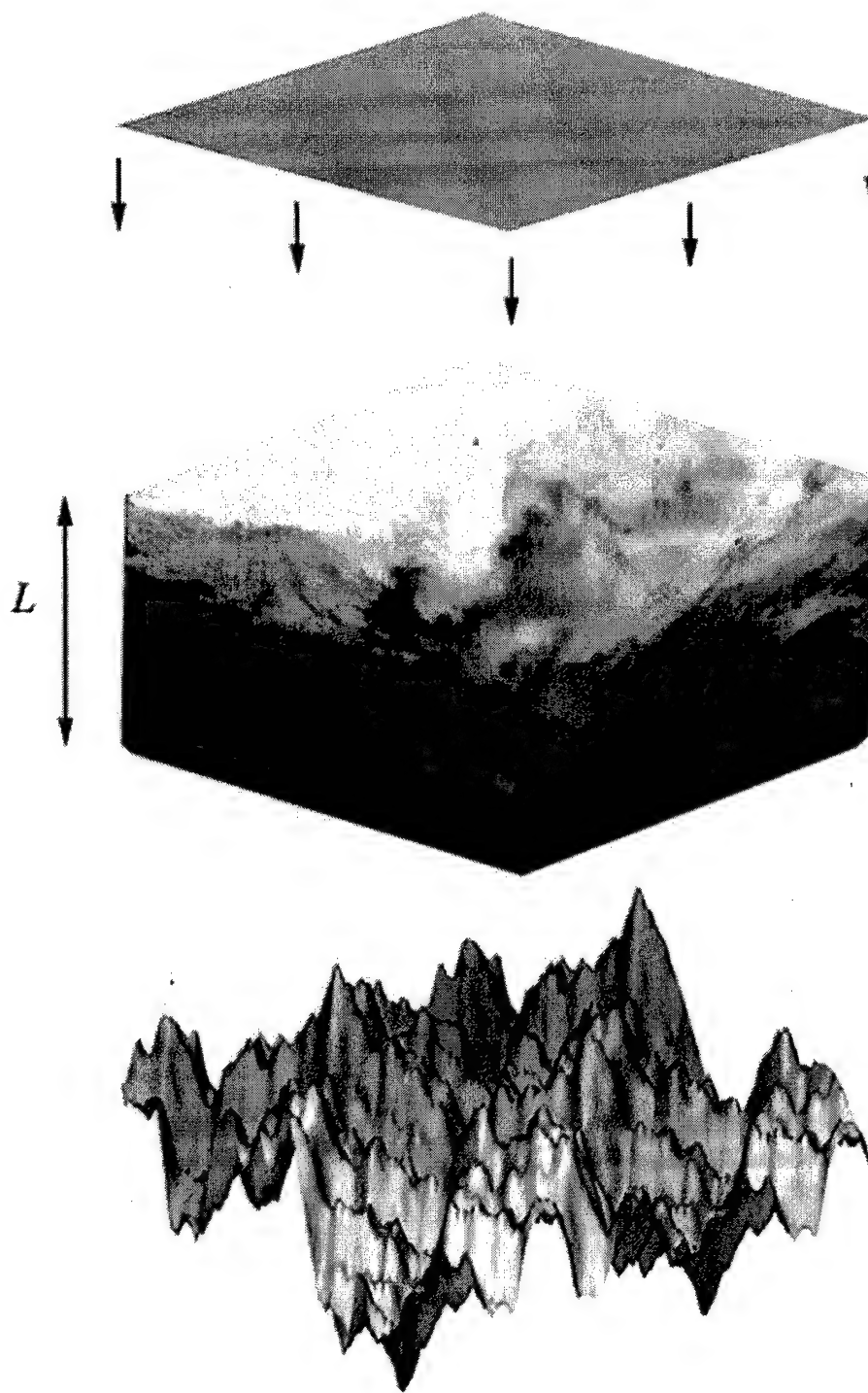
Figure 4b. Illustration of the anisotropic box-counting technique for the wavefront as shown in figure 3b.

Figures 5a, b, and c. Comparison of the coverage count, coverage fraction, and coverage dimension for the wavefront as shown in figures 3a and b. The dashed curves correspond to figure 3a, and the solid curves correspond to figure 3b. The differences at the small scales indicate that the small-scale behavior is sensitive to the choice of the AWA parameter.

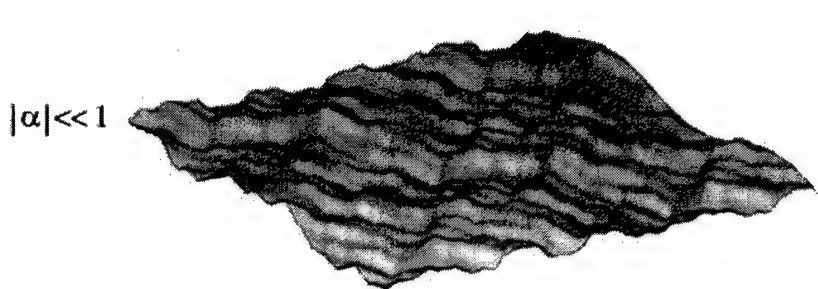
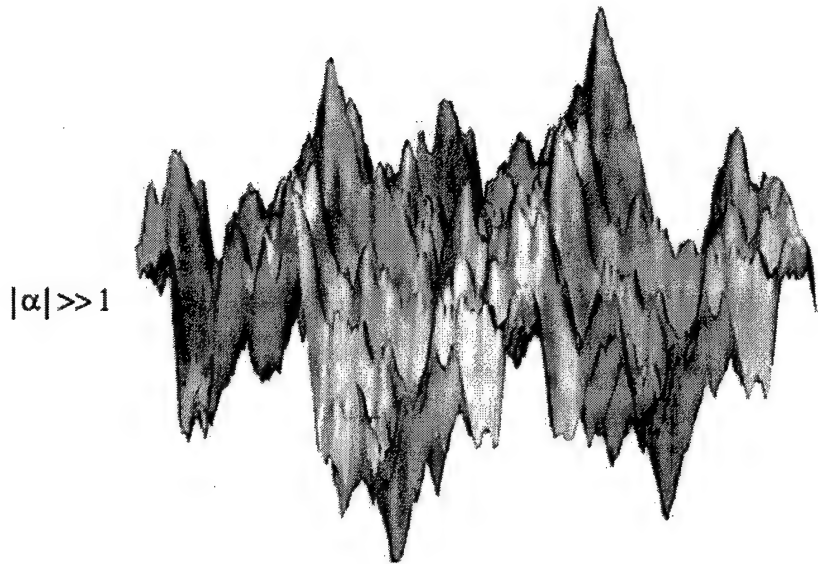
Figures 6a, b, and c. Examples of experimental wavefront OPD profiles,  $\text{OPD}(x)$ , derived from two-dimensional refractive-index field measurements in large-Reynolds-number ( $Re \sim 10^6$ ) high-compressibility ( $M_c \sim 1$ ) shear layers.<sup>2,14</sup> The OPD and spatial coordinate  $x$  denote normalized values. The normalization employs the transverse spatial extent of the shear layer and the ambient (freestream) refractive-index difference. The incident wavefronts are initially linear, i.e. straight, and propagate transverse to the flow, from one freestream to the other, through two-dimensional spatial streamwise slices of the flow. The wavefront OPD profiles correspond to the aerooptical wavefronts that emerge from the turbulent flow region.

Figures 7a, b, and c. Ensemble-averaged results for the instantaneous structure of wavefront OPD profiles in large-Reynolds-number ( $Re \sim 10^6$ ) high-compressibility ( $M_c \sim 1$ ) shear layers, cf. figures 6a, b, and c: (a) coverage function  $N_2(\lambda; \alpha^*)$ , (b) coverage fraction  $F_2(\lambda; \alpha^*)$ , and (c) relative coverage dimension  $D_2(\lambda; \alpha^*) - 1$ . The value of the critical AWA parameter  $\alpha^*$  for the results shown is  $\alpha^* \sim 0.9$ . The plateau in (c) indicates a clear presence of self-similarity of the anisotropic wavefront structure over a range of small scales spanning nearly a decade.

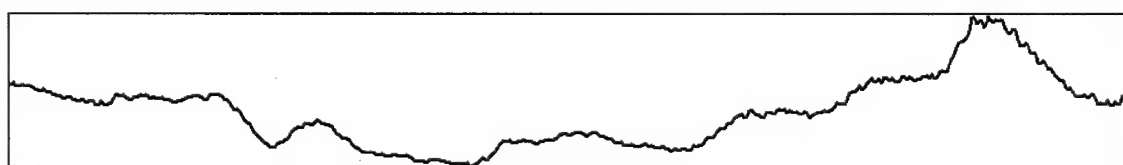
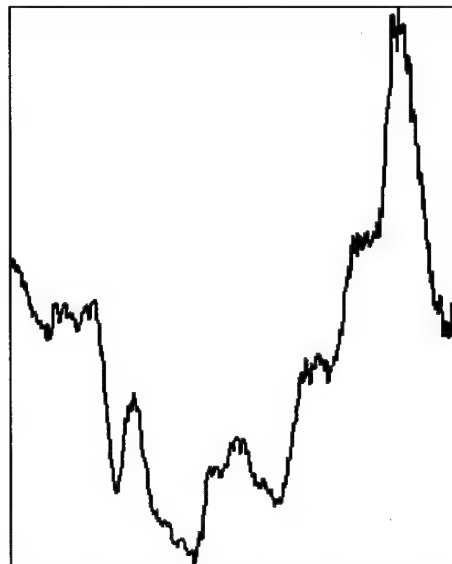
*AIAA Journal*, Catrakis, Aguirre, & Nathman, Figure 1



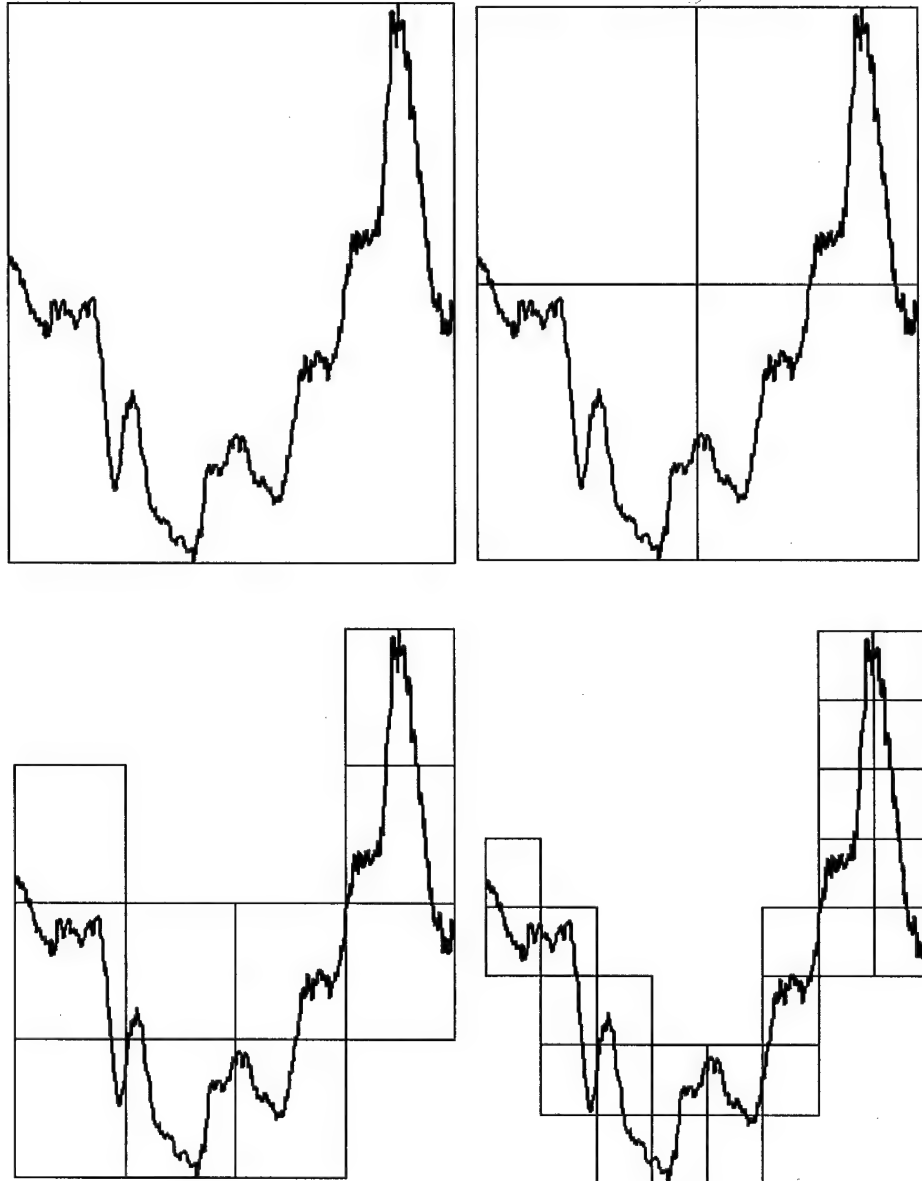
*AIAA Journal*, Catrakis, Aguirre, & Nathman, Figures 2a and b



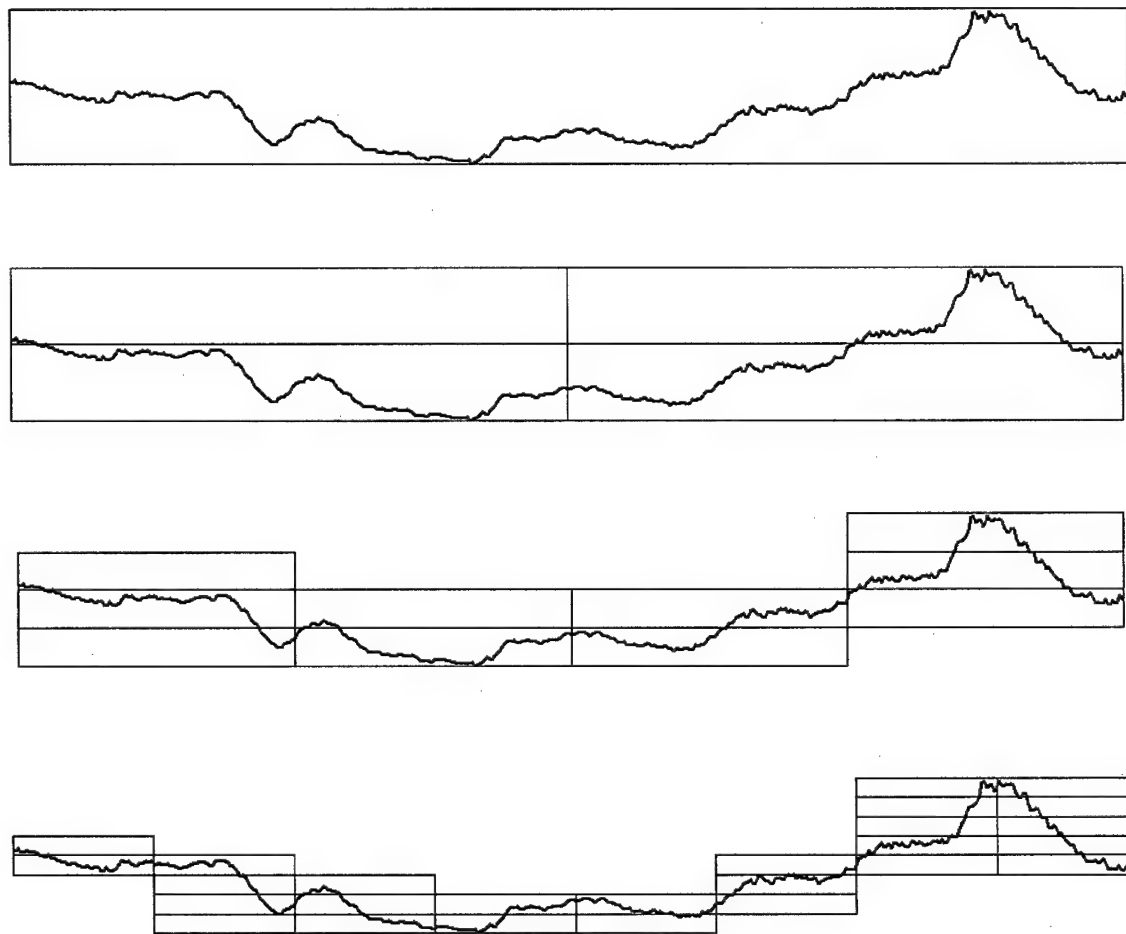
*AIAA Journal*, Catrakis, Aguirre, & Nathman, Figures 3a and b



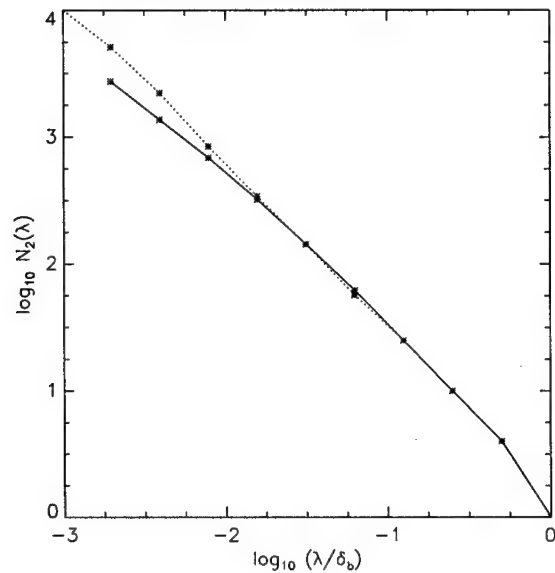
*AIAA Journal*, Catrakis, Aguirre, & Nathman, Figure 4a



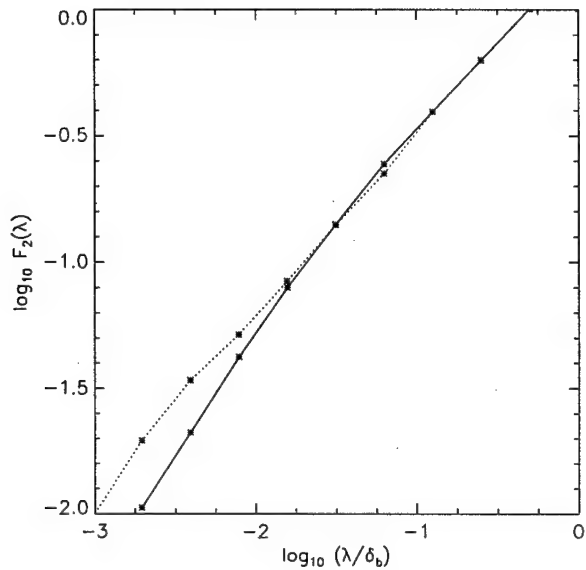
*AIAA Journal*, Catrakis, Aguirre, & Nathman, Figure 4b



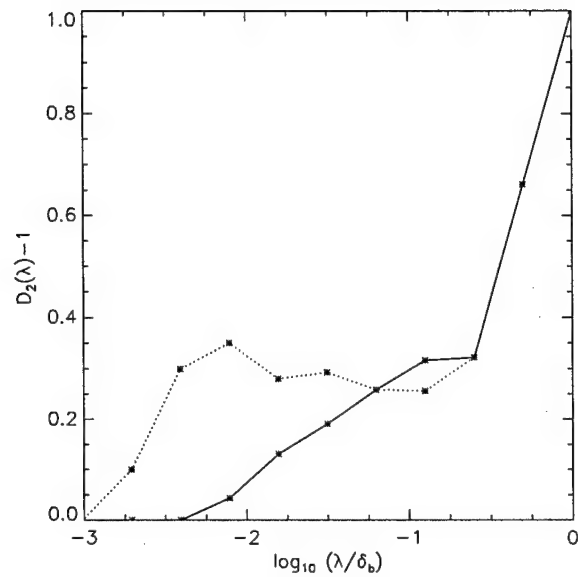
*AIAA Journal*, Catrakis, Aguirre, & Nathman, Figure 5a



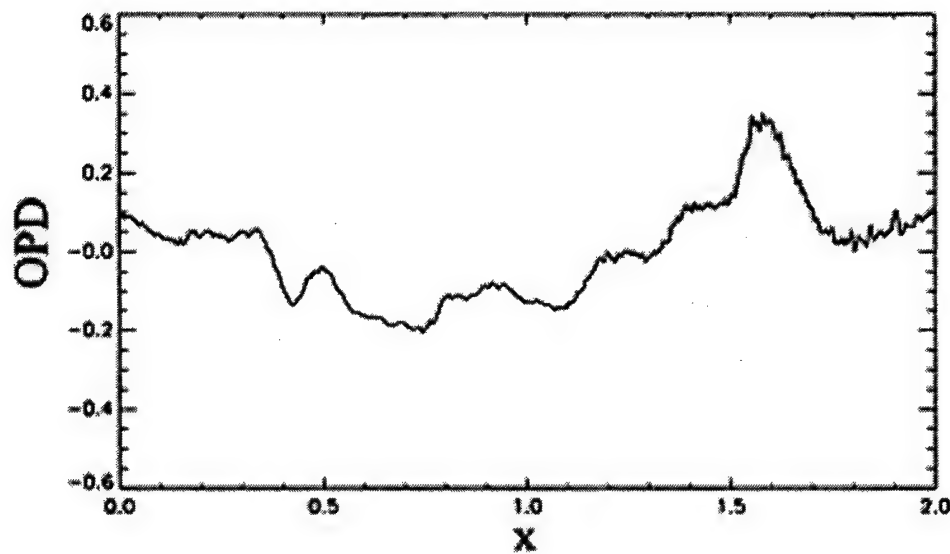
*AIAA Journal*, Catrakis, Aguirre, & Nathman, Figure 5b



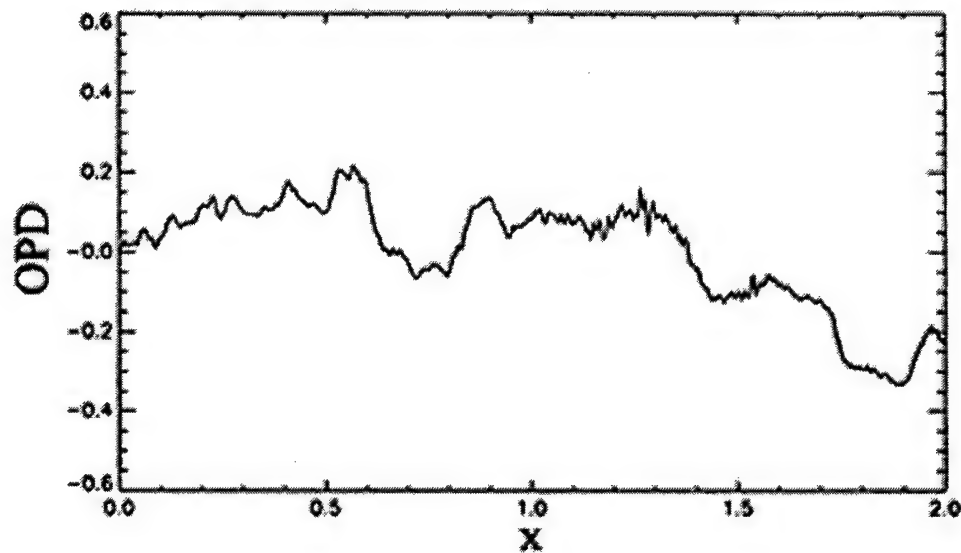
*AIAA Journal*, Catrakis, Aguirre, & Nathman, Figure 5c



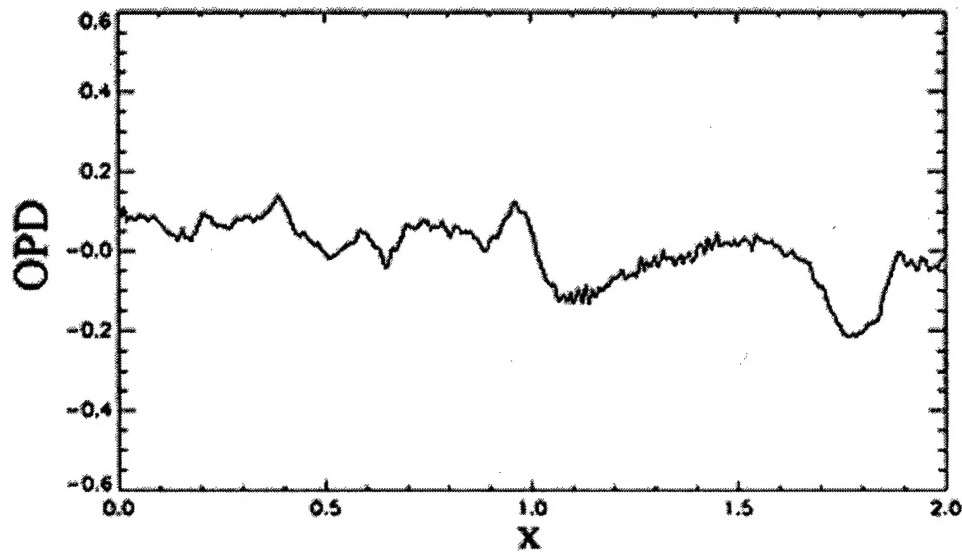
*AIAA Journal*, Catrakis, Aguirre, & Nathman, Figure 6a



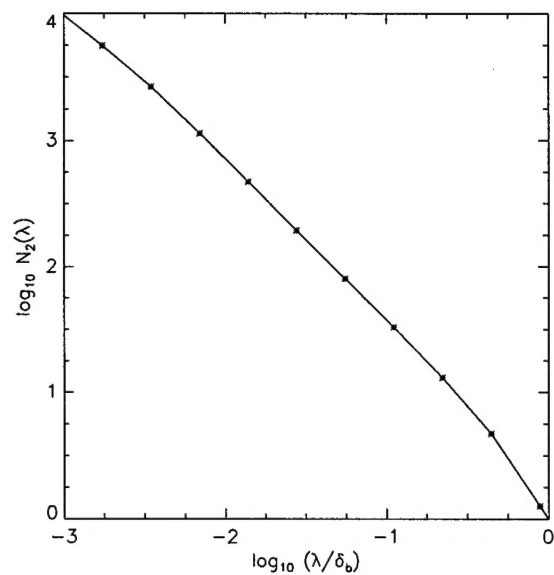
*AIAA Journal*, Catrakis, Aguirre, & Nathman, Figure 6b



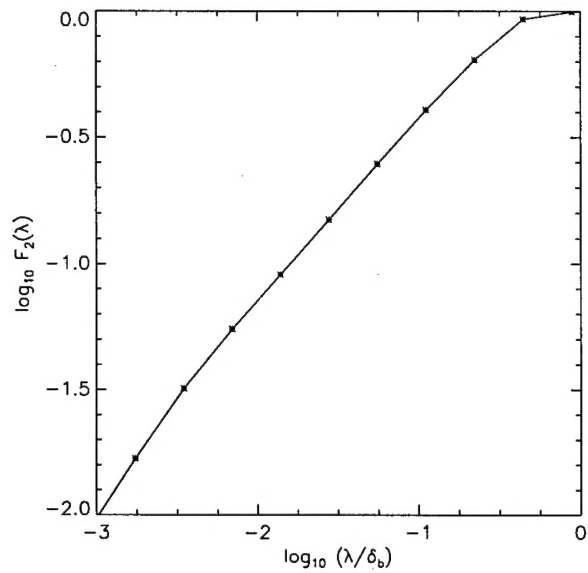
*AIAA Journal*, Catrakis, Aguirre, & Nathman, Figure 6c



*AIAA Journal*, Catrakis, Aguirre, & Nathman, Figure 7a



*AIAA Journal*, Catrakis, Aguirre, & Nathman, Figure 7b



AIAA Journal, Catrakis, Aguirre, & Nathman, Figure 7c

